#644
Earth Sc

STS-2/OSTA-1

TROPOSPHERIC CØ MIXING RATIO TAPE

81-111A-04A

ESAC-00013

Table of Contents

---

1. INTRODUCTION:

The documentation for this data set was originally on paper, kept in NSSDC's Data Set Catalogs (DSCs). The paper documentation in the Data Set Catalogs have been made into digital images, and then collected into a single PDF file for each Data Set Catalog. The inventory information in these DSCs is current as of July 1, 2004. This inventory information is now no longer maintained in the DSCs, but is now managed in the inventory part of the NSSDC information system. The information existing in the DSCs is now not needed for locating the data files, but we did not remove that inventory information.

The offline tape datasets have now been migrated from the original magnetic tape to Archival Information Packages (AIP's).

A prior restoration may have been done on data sets, if a requestor of this data set has questions; they should send an inquiry to the request office to see if additional information exists.

2. ERRATA/CHANGE LOG:

NOTE: Changes are made in a text box, and will show up that way when displayed on screen with a PDF reader.

When printing, special settings may be required to make the text box appear on the printed output.

Version	Date	Person	Page	Description of Change
01				
02				

3 LINKS TO RELEVANT INFORMATION IN THE ONLINE NSSDC INFORMATION SYSTEM:

http://nssdc.gsfc.nasa.gov/nmc/

[NOTE: This link will take you to the main page of the NSSDC Master Catalog. There you will be able to perform searches to find additional information]

4. CATALOG MATERIALS:

a. Associated Documents To find associated documents you will need to know the document ID number and then click here. http://nssdcftp.gsfc.nasa.gov/miscellaneous/documents/

b. Core Catalog Materials

B R I E F D E S C R I P T I O N
Tropospheric CO Mixing Ratio Tape
81-111A-04A ESAC-00013

This set of carbon monoxide values was archived by the principal investigator on magnetic tape that were created on an IBM 360 computer in ASCII format. The data set contains carbon monoxide mixing ratios that were inferred from radiances measured at 2080-2220 cm**-1. The column values cover an altitude range of 3-12 km and, horizontally, between 38 deg N. and 38 deg S. over all longitudes, with a precision of about 10%. The data agree to within 20-30% of near simultaneous aircraft measurements made over Australia.

M A T E R I A L S F O R D I S T R I B U T I O N
81-111A-04A
Tropospheric CO Mixing Ratio Tape

Middle and Upper Tropospheric Carbon Monoxide Mixing Ratios as Measured by a Satellite Borne Remote Sensor During November 1981 (38 pp. + tables, figures, and two appendices).

A preliminary assessment of results from the MAPS experiment on STS-2. Dec. 1981.

(CYN, 9/97)

A C K N O W L E D G E M E N T S

When using the data in any reports, publications, or presentations, please acknowledge the National Space Science Data Center.

REQ. AGENT
SAR

RAND NO.
V0328

ACQ. AGENT
CYN

STS-2/OSTA-1

TROPOSPHERIC CO MIXING RATIO TAPE

81-111A-04A

THIS DATA SET CATALOG CONSISTS OF TWO 9-TRACK, ASCII, 1600 BPI MAGNETIC TAPES. THE TAPES CONTAIN ONE FILE OF DATA EACH AND WERE CREATED ON AN IBM 360 COMPUTER. THE D AND C NUMBERS ALONG WITH THE TIME SPANS ARE AS FOLLOWS:

D#	C#	TIME SPAN
D-72286	C-25945	11/14/81
D-72287	C-25946	11/14/81

84-111A-04A

MEASUREMENT OF AIR POLLUTION FROM SATELLITES

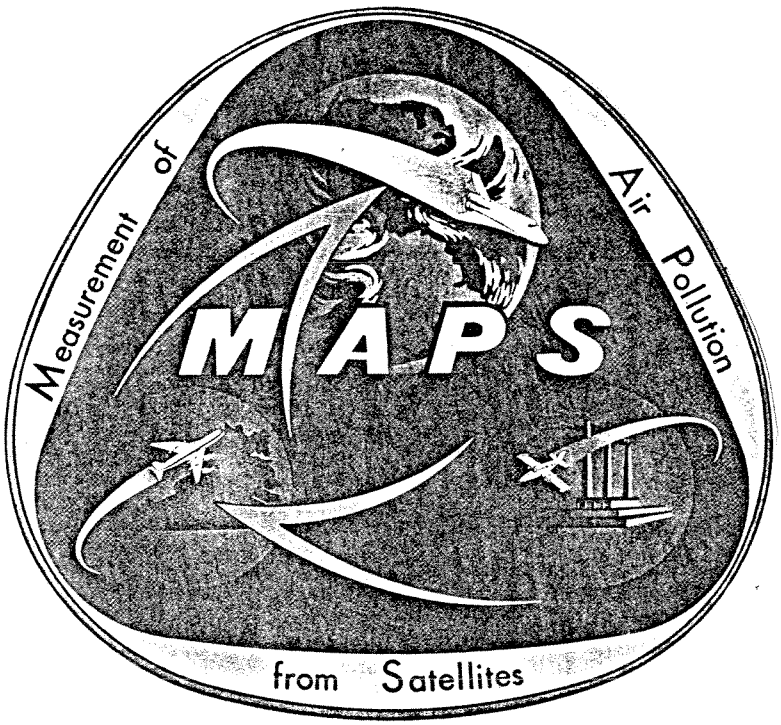

A preliminary assessment of results from the MAPS experiment on STS-2.

December 8, 1981

MAPS

On its second flight, the Space Shuttle carried its first science and applications payload, designated OSTA-1, to demonstrate the Shuttle's capabilities as a research platform. The MAPS experiment, one of five located in the payload bay, is aimed at providing the seasonal, global maps of carbon moxoxide that are needed to substantiate and provide insight into theories and mathematical models required to increase our understanding of atmospheric physics. The goal of the NASA Tropospheric Air Quality Program is to acquire sufficient understanding of the chemical and dynamic processes of the global troposphere so that man's impact on global air quality can be accurately assessed.

The experiment objectives may be divided into two general categories:

Scientific Objectives:

Measure the latitudinal and longitudinal distribution of carbon monoxide in the middle troposphere.

Verify the transport of carbon monoxide from the northern hemisphere to the southern hemisphere.

From this and subsequent missions, to study the seasonal dependence of this transport.

Observe and define the extent of interhemispheric air mass transport in the troposphere.

Technical Objectives:

Investigate and define the performance and operation characteristics of the sensor system.

Evaluate the operational difficulties involved in the accumulation, characterization, and evaluation of remote sensor data in a world-wide application.

Evaluate and refine the method of date inversion used for obtaining carbon monoxide concentration from sensor output.

Begin to evaluate the use of multiple, short-term Shuttle flights to compile a data set useful in the investigation of long-term changes in atmospheric composition.

From preliminary examinations of the data, the MAPS experiment was highly successfuly. After being powered up 4 hours, 25 minutues into the STS-2 mission, the instrument operated normally for about 42.5 hours, after which it was powered-down in preparation for de-orbit and landing. During operation, the instrument executed five self-calibration cycles, three automatically initiated and two on command from the ground. The instrument operated in the data collection mode for slightly more than 40 hours and it is estimated during 32-35 hours of that time, the spacecraft was in the proper attitude for Earth-viewing by the instrument.

Some preliminary examination assessments:

- Instrument response was stable despite larger-than predicted swings in the pallet temperature.
- The signal-to-noise ratio of the measurements meets or exceeds the prelaunch estimate of 80-to-1.
- Adequate viewing coverage was obtained over about 90% of the Earth's surface between 37 1/2° North and South latitudes.
- Approximately 20% of the observations occurred in long stretches of apparently cloud-free fields-of-view, averaging 4000 km (2500 miles) along the Shuttle ground track; these segments are expected to provide excellent quality measurements.

In addition to the measurements made by the shuttle instrument, several correlative aircraft underflights were carried out. Two of these flights occurred on the east coast of the United States where a jet aircraft supplied by Lewis Research Center and based at Langley Research Center carrying a prototype of the MAPS Shuttle instrument underflew orbits 18 and 21. Atmospheric samples were collected during these flights

in stainless steel cylinders at several altitudes between 41,000 feet and 1,000 feet to provide additional information about the distribution of pollutants. Similar atmospheric samples were obtained over the Eastern Pacific by an aircraft based at Ames Research Center which underflew orbits 21 and 22. A number of air samples were also obtained in the southern hemisphere through a joint effort of the Australian Commonwealth Scientific and Industrial Research Organizations (CSIRO) and the Oregon Graduate Center. The results of these correltive measurements will be compared with those made from the Shuttle as part of the data validation process.

In summary, it appears that sufficient data was obtained to achieve all of the technical objectives and 80-90% of the scientific objectives.

Current data reduction efforts are concentrated on verifying instrument calibrations and assembling the meteorological data required to infer carbon monoxide concentrations from the MAPS data.

The MAPS experiment is being conducted by Principal Investigator Henry G. Reichle, Jr. of NASA Langley Research Center and a science team consisting of the following:

Sherwin M. Beck
NASA/LaRC

William L. Chameides
Georgia Institute of Technology

W. Donald Hesketh
NASA/LaRC

Robert Lamontagne
Naval Research Laboratory

Claus B. Ludwig
Photon Research, Ins.
(La Jolla, CA)

Reginald E. Newell
Massachusetts Institute of Technology

Leonard K. Peters
University of Kentucky

Wolfgang Seiler
Max Planck Institude for Chemistry at Maintz

H. Andrew Wallio
NASA/LaRC

Middle and Upper Tropospheric Carbon Monoxide Mixing Ratios as Measured by A Satellite Borne Remote Sensor During November 1981

Henry G. Reichle, Jr., Vickie S. Connors, J. Alvin Holland, Warren D. Hypes, and H. Andrew Wallio

Atmospheric Sciences Division
NASA Langley Research Center

Joesph C. Casas, Barbara B. Gormsen, and Mary S. Saylor

Old Dominion University

Wilfred D. Hesketh

Air Force Rocket Propulsion Laboratory

Short title: Tropospheric Carbon Monoxide Mixing Ratios

********* APPENDIX 2 Contains a description of the magnetic tapes.

Encl. 1

Introduction

Carbon monoxide (CO) is a photochemically active gas on the global scale in the troposphere. To date, the general features of its distribution have been determined by a combination of surface based direct measurements [Robinson and Robbins, 1968; Lamontagne et al., 1971; and Swinnerton and Lamontagne, 1974]; aircraft-borne direct measurements [Seiler and Junge, 1970; Seiler and Warneck, 1972; Seiler, 1974; Newell and Gauntner, 1979; Reichle and Condon, 1979; Heidt et al., 1980; Seiler and Fishman, 1981; Newell et al., 1981; Rasmussen et al., 1982]; surface-based remote measurements [Shaw, 1958; Dianov-Klokov et al., 1975]; and aircraft-borne remote measurements [Doherty et al., 1986]. These measurements indicate that there is more CO in the northern hemisphere than in the southern hemisphere with the maximum values being found near the surface at northern midlatitudes. In general, the CO mixing ratio decreases with altitude in the northern hemisphere, and it has a free tropospheric average value in the range of 120 ppbv near 45°N. In the southern hemisphere, the gas tends to be more nearly uniformly mixed with a value of about 60 ppbv near 45°S.

The sources and sinks of CO are thought to be known, although there is a very large uncertainty in the relative magnitudes of the various sources. It appears that the magnitude of the anthropogenic sources (primarily agricultural burning and fossil fuel use) is approaching the magnitude of the natural sources (primarily the oxidation of methane and nonmethane hydrocarbons). The primary sink is thought to be photochemical oxidation with a small contribution by soil uptake. A detailed discussion of the photochemistry, sources, and sinks of CO is found in Logan et al. [1981].

This document presents a preliminary discussion of the results of a nadir-viewing space shuttle experiment designed to measure remotely the global distribution of middle and upper tropospheric CO. The experiment was entitled "Measurement of Air Pollution from Satellites" (MAPS), and it was flown on the second engineering test flight (STS-2) of the shuttle in November 1981. Preliminary results for a portion of one orbit have been previously reported [Reichle et al., 1982]. This paper reports all of the usable data obtained during the flight and presents information on the precision and accuracy of the data. Highlights of the experiment, the instrument technique and calibration, and the data reduction procedures are presented to support the data. An overview of the payload is presented in Settle and Taranik [1982].

The MAPS Experiment

The OSTA-1 MAPS experiment flown on STS-2 evolved from laboratory studies, aircraft test flights, and analytical modeling [Acton et al., 1973; Ludwig et al., 1974; Hesketh et al., 1977; Reichle et al., 1986]. The instrument uses the gas filter correlation (GFC) technique to maintain high radiation throughput and high effective spectral resolution in the 4.67-μm fundamental band of CO. As shown schematically in Figure 1, the upwelling radiation is gathered by the foreoptics and is directed through a system of gas cells to the detectors. The output of the detector behind each gas filled cell is subtracted from the output of the detector behind the vacuum cell. This difference signal is strongly related to the degree of correlation between the spectrum of the gas contained in the gas filled cells and the spectrum of the upwelling radiation. Changing the path length and the pressure of the gas in the cells causes the altitude from which the strongest signal is received to be shifted vertically in the

atmosphere. This then allows the atmosphere to be probed with some degree of vertical resolution. As can also be seen from Figure 1, the output of the detector behind the vacuum cell is simply that of a broadband radiometer, and its output is most sensitive to the radiation received from the underlying surface.

The characteristics of the instrument flown on STS-2 are shown in Table 1. The 4.33° field-of-view of the radiometer achieves an instantaneous field-of-view at the surface of approximately 20 km by 20 km from the space shuttle altitude of 260 km. The instrument is similar in principle to the selective chopper radiometer [Abel et al., 1970]; however, it continuously maintains a balanced condition using a technique described by Ward and Zwick [1975]. It had three channels. One channel, called the ΔV or the high pressure channel, was most sensitive to CO in the middle troposphere. The second gas channel, called the $\Delta V'$ or low-pressure channel, was most sensitive to CO in the upper troposphere or lower stratosphere. The third channel, called the V channel, was primarily influenced by the temperature of the surface of the earth.

Signal Function

The primary source of the radiometric signal is the thermal radiation emitted by the earth-atmosphere system; thus, the technique is inherently nonuniform in its response to carbon monoxide located at different altitudes in the atmosphere.

For the MAPS instrument, the theoretical radiance at the detectors, ΔL and L, can be expressed as

$$\Delta L = \int_{\Delta\tilde{\nu}} L_T(\tilde{\nu})[\tau(\tilde{\nu})_{gas} - \tau_{vac}]F d\tilde{\nu}, \tag{1}$$

and

$$L = \int_{\Delta\tilde{\nu}} L_T \tau_{vac} F d\tilde{\nu} \tag{2}$$

where $\Delta\tilde{\nu}$ = the spectral bandpass of the instrument in wavenumber

$L_T(\tilde{\nu})$ = the total monochromatic upwelling radiant energy

$\tau(\tilde{\nu})_{gas}$ = the monochromatic transmission of the gas cell

τ_{vac} = the effective transmission of the vacuum cell, and

F = the instrument response function.

For a cloud-free nonscattering atmosphere under local thermodynamic equilibrium, the atmospheric radiative transfer equation for the total monochromatic upwelling radiant energy $L_T(\tilde{\nu})$ as viewed by a nadir-type sensor can be written as

$$L_T(\tilde{\nu}) = \varepsilon(\tilde{\nu})L^0(\tilde{\nu},T_s)\tau(\tilde{\nu},h') + \int_0^h L^0[\tilde{\nu},T(z)]\,\frac{d\tau(\tilde{\nu},z)}{dz}\,dz$$

$$+ \frac{1}{\pi}[1 - \varepsilon(\tilde{\nu})]\cos\theta H_s(\tilde{\nu})[\tau(\tilde{\nu},h)][\tau(\tilde{\nu},h')]^{f(\theta)}, \qquad (3)$$

where $\varepsilon(\tilde{\nu})$ = the wavenumber dependent surface emittance, and

$L^0(\tilde{\nu},T)$ = the Planck blackbody function, which is dependent on wave number and surface temperature T_s, or the radiating gas temperature at a particular altitude $T(h)$.

The monochromatic transmittance of the atmosphere between the emitting surface at altitude z and the altitude of the sensor h is represented by $\tau(\tilde{\nu},h)$, and the monochromatic vertical transmission of the entire modeled atmosphere is represented by $\tau(\tilde{\nu},h')$. The solar zenith angle is θ, and the wave number-dependent solar irradiance at the top of the atmosphere is H_s. The Chapman function $f(\theta)$ is equal to $\sec\theta$ for $0° \leq \theta \leq 60°$ and is equal to the Chapman polynomial for $\theta > 60°$. The three terms on the right-hand side of Equation 3 represent, respectively, the thermal radiation emitted by the surface and transmitted through the atmosphere to the sensor, the thermal

radiation absorbed and emitted by the atmosphere, and the solar radiation transmitted through the entire atmosphere, reflected by the surface, and transmitted through the atmosphere to the altitude of the sensor.

If Equation 3 is substituted into Equation 1, it can be rewritten as

$$\Delta L = \int_{\Delta\tilde{\nu}} \int_{0}^{h} a(x)\tau^{z,h}(G - L_A)(\tau_{gas} - \tau_{vac})Fd\tilde{\nu}dz \qquad (4)$$

where $a(x)$ = the absorption per unit length

$\tau^{z,h} = \exp\{-\int_{z}^{h} a(x)dx\}$,

$G = \varepsilon_S(\tilde{\nu})L^0(\tilde{\nu},T_S)$, and

L_A = the Planck function for the atmosphere at temperature $T(z)$.

The solar terms have been omitted for ease of discussion. Assuming hydrostatic equilibrium and perfect gases, Equation 4 can be rewritten as

$$\Delta L = \int_{\Delta\tilde{\nu}} \int_{p_s}^{0} a(p)\tau^{p,o}[G - L_A(T(p))][\tau_{vac} - \tau_{gas}]Fd\tilde{\nu}[\frac{RT(p)}{mg}]\ d(\ln p) \qquad (5)$$

where R = the universal gas constant,

p = the atmospheric pressure,

g = the acceleration due to gravity, and

m = molecular weight

We define a signal function (SF) such that

$$\Delta L = \int_{p_s}^{0} SF\ \ d(\ln p) \qquad (6)$$

The signal function then describes the relative contribution at each point p to the total signal received from the atmosphere. The signal function is then

$$SF = \int_{\Delta\tilde{\nu}} a(p)\tau^{p,o}[G - L_A(T(p))][\tau_{vac} - \tau_{gas}] \frac{RT(p)}{mg} F d\tilde{\nu} \qquad (7)$$

The most important characteristics of the instrument are set during its design, and they are summarized in the product $[\tau_{vac}-\tau_{gas}]F$. The function F describes the overall broadband transmission properties of the instrument. It is primarily controlled by an interference filter that has a bandpass between 2070 and 2220 cm^{-1}. Within this bandpass the transmission is high and nearly uniform; outside this bandpass the transmission is essentially zero. The effects of long-wavelength transmission leakage of the filter are removed by the very low sensitivity of the PbSe detector at long wavelengths. The wings of the CO band were cut off to reduce the interference effect of N_2O and CO_2. During actual data reduction, the function F is described by a measured response function of the instrument. The term $(\tau_{vac}-\tau_{gas})$ describes the characteristics of the 1-cm long gas cells and the instrument balance gain. Its value varies rapidly from about -0.1 to +0.9 as a function of wavenumber. (The balancing process, in effect, sets $\tau_{vac} = \overline{\tau}_{gas}$.) Because the absorption lines of CO are widely spaced (about 4 cm^{-1} between line centers) and are rather narrow (the halfwidth of the CO lines in the higher pressure cell is about 0.02 cm^{-1}), the difference $\tau_{vac}-\tau_{gas}$ is near 0 over most of the band and approaches 1 at the line centers. The net effect is to strongly weight the signal function to the spectral region near the line centers.

The terms describing the atmosphere and the surface are $[G-L_A(T(p))]$, $a(p)$, and $\tau^{p,o}$. $[G-L_A(T(p))]$ describes the relationship between the radiation received from the surface and that received from the atmospheric layer at the pressure p. If an atmospheric layer is at the same temperature (or more precisely, emitting the same amount of radiation) as the surface,

then the signal will contain no information from that layer. In the atmosphere, the surface and the air near the surface are usually at nearly the same temperature. The difference between the temperatures increases with altitude since the atmospheric temperature usually decreases with height. Because the temperature contrast is about 0 near the surface, this term should drive the signal function toward 0 at the surface. Because of the previously stated characteristics of the (τ_{vac}-τ_{gas}) term, the properties of the two remaining atmospheric terms near the CO line centers will be most important in determining their contribution to the signal function. Near the line centers $\tau_{P,O}$ peaks in the upper atmosphere, while the absorption per unit length, a(p), is maximum near the surface and decreases exponentially with height. The net result of the integration over wavenumber of the product of these terms for reasonable values of atmospheric, surface, and instrument conditions is a function that is small near the surface and that increases to a maximum value within the troposphere, then decreases as the upper limit of the atmosphere is approached. The shape of the signal function is somewhat influenced by the amount and distribution of CO within the atmosphere; however, for the data reported here, these effects are small.

Figure 2 shows signal functions calculated for a model atmosphere containing 110 ppbv of CO uniformly distributed in the vertical for the two different cell conditions (76 torr and 266 torr CO) that were flown on this experiment. It can be seen that both signal functions are broad and that there is considerable overlap between them. It is clear, however, that the lower pressure channel does peak at a higher altitude, and its signal will be

more strongly influenced by the stratosphere at midlatitudes. In the tropics where the tropopause is higher, both channels should be sensitive to tropospheric CO. Since neither channel is very sensitive to CO in the mixing layer (the lower 2 to 3 km of the atmosphere), the data reported here are representative of the free troposphere and the lower stratosphere.

Instrument Operation

A diagram of the instrument flown on STS-2 is shown in Figure 3. Radiation emitted by or reflected from the surface of the earth is directed by a pointing mirror into the objective lens of the radiometer. As it passes through the atmosphere, the radiation is modified through selective absorption by the infrared active gases present. After being gathered by the objective lens, the radiation is chopped against a temperature controlled reference blackbody (BB-1). The chopped beam then passes through the field stop, a broadband filter (2080 to 2220 cm^{-1}), and a beam combiner to a system of beamsplitters. These beamsplitters divide the energy among three detectors that are placed behind three corresponding gas cells. The gas cell before the V channel detector is filled with helium at 76 torr (1Torr = 133.3 Pa). The 1-cm long gas cell before the ΔV detector is filled with CO at a pressure of 266 torr and helium at 2 torr. The 1-cm long gas cell before the $\Delta V'$ detector is filled with 76 torr of CO and 2 torr of helium. The helium is placed in the cells to aid in leak detection during cell construction. Because the three detectors "see" the same scene at the same time, the effect of scene brightness variation--induced by spacecraft motion, for example--is minimized. The output of the three detectors is amplified and passed on to differencing amplifiers that form the three outputs (ΔV, $\Delta V'$, and V) of the instrument. As can be seen from the foregoing, the operation of the two gas channels, ΔV and $\Delta V'$, is identical in principle. The two channels do differ slightly in that the radiation reaching the ΔV detector has undergone two

transmissions through the beamsplitters as opposed to the two reflections undergone by the energy reaching the $\Delta V'$ detector. This causes the two channels to respond differently to polarized light or to thermal drifts.

A significant consideration in the design and implementation of a gas filter radiometer is the establishment and maintenance of a stable zero condition for the gas channels. While the electrical output will not, in general, be zero volts for zero radiometric input (this in itself is not a problem--it simply represents a bias offset to be removed from the signals), it should not be too large and it should be stable both as a function of target temperature and instrument temperature. This stable condition is best achieved by operating the instrument in what is called a balanced mode. To achieve this mode of operation, one arranges either a mechanical attenuator in the V channel detector leg of the radiometer or an amplifier in the gas channel leg in such a way that the output of the instrument (ΔV or $\Delta V'$) is the same when either of the two blackbody targets is placed in the field-of-view of the radiometer. The temperatures of these targets are selected so that one is near the upper end of the range of expected scene temperatures and the other is near the lower end of that range. This then creates a condition in which the instrument output is nearly independent of scene temperature.

In the MAPS instrument, the balance condition is achieved by adjusting the gain of an amplifier in the gas cell leg of the instrument. This allows the two gas channels to be balanced independently. The initial balance is achieved by causing the radiometer to look alternately at the external balance cold blackbody (BB-5) and the external balance hot blackbody (BB-6) by means of the pointing mirror. After iterating the balance adjustment three times, the mirror exposes the calibrate blackbody-gas cell combination to the radiometer and then rotates so that the radiometer views the scene. This

process is repeated at 12-hour intervals by means of an internal timer, or as often as desired by command from the ground. At the completion of the three iterations, the instrument will be accurately balanced (assuming that the instrument temperature is stable during the balance cycle) generally to within the noise level. At that time, an internal automatic gain control (AGC) circuit senses the difference signal received at the detectors from the internal balance blackbodies, BB-2 and BB-3, which are being chopped at twice the scene chopping frequency. The AGC circuit then maintains this difference during the time period until the next rebalance by continuously adjusting the gain of an amplifier in the gas cell leg of the ΔV and $\Delta V'$ channels, thus maintaining the balanced condition.

Because a mirror was used to view the balance targets, the balance condition was not properly met during the flight, and, as a result, the output is dependent on the ground temperature. This will be seen later in the sections of this paper on instrument calibration and data reduction. The instrument is now being modified to correct this situation.

Flight Instrument

The four subassemblies of the flight instrument package shown in Figure 4 include the following: the optics subassembly which contains all of the optical elements, blackbodies, gas cells, detectors, preamplifiers, and a balance/calibrate unit; the electronics subassembly which houses the signal processing and control circuits, data handling circuits, balance/calibrate circuits, mode sequencing and control circuits, and power conditioning circuits; the flight magnetic tape recorder subassembly which records all of the scientific and housekeeping data during the mission; and the aerial camera subassembly which provides correlative cloud cover photographs of the subsatellite ground track during daylight portions of flight.

The subassemblies are mounted on a common baseplate. Thermal control of the MAPS instrument is achieved by conduction at the baseplate-shuttle pallet cold plate interface. After 4 to 5 hours of pallet coolant loop operation at a constant temperature, the MAPS optics unit reaches an equilibrium temperature that is less than 2 K warmer than the pallet cold plate temperature. A multilayer insulation cover isolates the experiment from the thermal environment of space and from the electromagnetic radiative interference produced by the shuttle.

Instrument Calibration

The calibration of the instrument was carried out in three parts. Prior to the flight it was calibrated in the laboratory at room temperature. Following the flight, the instrument was calibrated in a thermal vacuum chamber at a variety of instrument temperatures. During the flight, data that allowed the determination of the zero position were acquired while the instrument was viewing deep space.

Preflight

The MAPS instrument preflight calibration tests were carried out in a laboratory at an ambient temperature of 298 K. These tests determined the magnitude of the output noise, the radiometric responsivity, the degree of linearity of the output signal response, voltage offsets, and the repeatability of the instrument for each of the three channels, V, ΔV, and $\Delta V'$. These results served as a baseline for determining instrument long-term stability.

The ground calibration system, which was specially designed for the MAPS experiment, independently controls the composition, total pressure, and temperature of the gas mixture contained in a 0.5-meter long calibration cell. In addition, the temperature of the high quality calibration blackbody,

ε = 0.997, can be independently controlled between 238 K and 345 K. In the calibration tests, the values of these parameters were varied over ranges which bracketed the expected range of atmospheric conditions. The measured temperatures and pressures of the gas mixtures, blackbody target temperatures, instrument output voltages, and other housekeeping signals were recorded during each step of the calibration testing procedure.

The recorded data were used in conjunction with a line-by-line radiative transfer program to compute the instrument radiometric calibration constants. For a given set of test conditions, this computer program calculated the radiance values, L, ΔL, and ΔL', which corresponded to the test conditions for each of the measured signal output voltages of the three instrument channels, V, ΔV, and ΔV'.

The V channel calibration constants, R and β, for each instrument mainframe temperature, which is known to be the same as TBB2, were determined by the least squares solutions to the calibration test data such that

$$V = [R^{V}(TBB2)][L_{target} - L_{BB1}] + \beta(TBB2) \qquad (8)$$

where $R^{V}(TBB2)$ is the responsivity (volts/watt cm^{-2} sr^{-1}) and $\beta(TBB2)$ is the offset voltage. The total inband radiances for the target blackbody L_{target} and for the internal reference blackbody, L_{BB1}, were calculated using the line-by-line radiative transfer calculations.

The relationship between the output voltage signals for the ΔV and ΔV' channels and the target radiometric signals ΔL and ΔL' is given by

$$\Delta V_{target} = [R^{\Delta V}(TBB2)][\Delta L_{target}] + \Delta V_{ref}(V,TBB2) \quad (9)$$

$$\Delta V'_{target} = [R^{\Delta V'}(TBB2)][\Delta L'_{target}] + \Delta V'_{ref}(V,TBB2) \quad (10)$$

where $R^{\Delta V}(TBB2)$ and $R^{\Delta V'}(TBB2)$ are the instrument temperature dependent responsivities,

ΔL_{target} and $\Delta L'_{target}$ are the calculated scene radiances for the ΔV and $\Delta V'$ gas channels, respectively, and

$\Delta V_{ref}[(V,TBB2]$ and $\Delta V'_{ref}[V,TBB2]$ are the zero reference offset balance voltages for the ΔV and $\Delta V'$ channels.

The magnitude of the offset voltages is dependent both on the instrument temperature, TBB2, and on the magnitude of the target radiance as indicated by the V channel output signal, V.

The performance of the MAPS instrument during the preflight time period was very stable. The repeatability of the calculated calibration constants was better than ±2 percent for testing performed at approximately the same instrument temperature. The noise level on all three channels remained constant at the levels shown in Table 1.

Postflight

The large variation in coolant loop temperature encountered during the flight necessitated an extensive set of postflight tests and calibrations to characterize the instrument as a function of instrument temperature. The calibrations were carried out in a cryogenically pumped chamber capable of achieving a pressure of 1×10^{-7} torr. The instrument was mounted on a heat transfer baseplate and supported by a hanging fixture mounted to the upper rail of the chamber. The camera was removed and replaced by a secondary gas calibration reference cell and secondary standard blackbody apparatus which

permitted the gas cell to be inserted and removed from the space between the optical port of the instrument and the secondary standard blackbody.

The baseplate and secondary standard blackbody were connected to external thermal control units so that their temperatures could be varied independently. Thermistors similar to the internal thermistors of the MAPS experiment were used to measure the temperature of the secondary standard blackbody and the temperature of the 2.12-cm long secondary standard reference gas cell. The list of test conditions is detailed in Table 2. Six different temperatures of the secondary standard blackbody were run, the maximum standard deviation for each temperature being less than ±0.03 K. The gas cell temperature was 8 K to 10 K higher than the instrument temperature. The instrument temperature was set to four different values which spanned the temperatures encountered during the OSTA-1 mission. The maximum standard deviation for each of the instrument temperatures, TBB2, was less than ±0.12 K. Three different gas mixtures of CO in N_2 were used in the calibration process.

The results from the entire set of test conditions were used to determine the calibration constants for the instrument. The procedure for determining the calibration constants was similar to the one previously described for the preflight laboratory calibration procedure. Figures 5, 6, and 7 show examples of the instrument output for various target temperatures and the responsivities and offsets as a function of instrument temperature for each of the three channels of the instrument. It can be seen from these figures that the output of each channel was an essentially linear function of the input singal. The responsivity, i.e., the slope of the calibration curves, varied nearly linearly as a function of instrument temperature as is shown in the (b) section of the three figures. It is clear, however, from Figures 6(c) and

7(c) that the zero offsets of the ΔV and $\Delta V'$ channels, in addition to being a function of the instrument temperaure, were non-linearly related to the V channel signal.

Inflight

As noted earlier, the MAPS instrument was exposed to very large coolant loop temperature variations during the STS-2 mission. These variations were so large and so rapid that it was not possible, in general, for the instrument to achieve a proper balanced condition during the 22-minute balance cycle. Only during the fourth rebalance attempt, which occurred about 13 hours before the end of the mission, was a good balance achieved. The data reported later in this paper were acquired between this fourth rebalance and the fifth rebalance.

The instrument temperature was almost the same during the fourth and fifth on-orbit balance/calibrate cycles, and it was nearly constant during the rebalance cycles; however, the instrument temperature varied between 277 K and 285 K during the data acquisition period between these two balance/calibrate cycles. Because the zero reference signal changes as the instrument temperature deviates from the balance temperature, it was necessary to determine the zero reference signal as a function of instrument temperature for the period between the fourth and fifth balance/calibrate cycles. This was accomplished by using data acquired while the instrument was viewing deep space, which is a known and stable source.

During this data acquisition period, three different sets of space viewing data were acquired. The first two data sets occurred shortly after the completion of the fourth balance/calibrate cycle, while the third space viewing data set was acquired some 10 hours later, just prior to the fifth on-orbit balance/calibrate cycle. The space viewing data were acquired for

instrument temperatures in the range of 277 K to 284 K. Figures 8 and 9 are plots of the ΔV and $\Delta V'$ voltages measured during the space viewing data time periods as a function of the instrument temperature, TBB2. As shown in Figures 8 and 9, the ΔV and $\Delta V'$ data acquired during the third space viewing data time period, i.e., for TBB2 greater than 282 K, appear to shift by a maximum of -50 millivolts for ΔV and by -33 millivolts for $\Delta V'$. The cause of this shift is unknown. It introduces an uncertainty of about 6% in the inferred CO values.

In addition to the ΔV and $\Delta V'$ space viewing data, the V channel signal during these time periods was needed to characterize the zero reference signals, ΔV_{ref} and $\Delta V'_{ref}$, as a function of scene radiance and instrument temperature. However, the data system for the V channel was saturated when the instrument viewed low radiance targets such as deep space. Therefore, a V channel output signal, i.e., the output voltage that would have been recorded had the data system not saturated, was calculated for instrument temperatures ranging from 276 K to 286 K using a target radiance, L_{target}, equivalent to that of deep space and the responsivities R(TBB2) and the offset voltages β(TBB2) that had been determined from the calibration data.

During the fourth balance cycle, the instrument temperature was approximately 282 K. It is a characteristic of the instrument that, for targets having a temperature near that of the external hot target, which is at 320 K, the ΔV and $\Delta V'$ zero reference levels do not change from the balance value as the instrument temperature changes. This characteristic, the data acquired during space viewing periods, i.e., zero reference level as a function of instrument temperature, and the mathematical form of the curves of zero reference signal level versus V channel output as determined during the vacuum chamber tests were combined to construct a family of curves of zero

reference level for the ΔV and $\Delta V'$ channels. These curves encompassed the ranges of instrument temperature and target radiance that were encountered between the fourth and fifth balance cycles. They are shown in Figures 10 and 11, and they form the basis for calculating the zero reference voltages used for the reduction of the data.

Data Reduction

The major steps in the method used to infer the CO mixing ratio from the data acquired by the MAPS experiment are shown in Figure 12. In this diagram the boxes indicate intermediate or final products, while the connecting arrows indicate some process or procedure for obtaining the next product.

The method of inferring the CO mixing ratios reported here is a modified form of that given by Wallio et al. (1983). The solution is based on a set of regression coefficients which describe the CO mixing ratio as a function of the radiances, L and ΔL

$$CO_{\text{mixing ratio}} = \sum_{i,j} B_{ij}(L)^i(\Delta L)^j \qquad (11)$$

where the regression coefficients B_{ij} are determined from a rigorous line-by-line radiative transfer calculation for a given atmosphere and variable surface conditions. The CO mixing ratio determined by this method is that value which, if uniformly mixed through the atmosphere, would produce the observed signals, L and ΔL.

The coefficients B_{ij} in Equation 11 are determined by the variables which describe the atmospheric state over which the instrument is measuring the radiances L and ΔL. It can be seen in Equation 7 that $T[p]$ predominantly describes the state of the atmosphere within the footprint of

the instrument. Because the MAPS experiment did not measure the atmospheric temperature, it was obtained from an independent source, the U.S. Navy Fleet Numerical Oceanography Center (FNOC) meteorological analyses (James Zuver, personal communication 1981). To incorporate the atmospheric temperature into the regression method, it was necessary to describe the temperature profile in terms of a single parameter.

The temperature parameter is the signal function weighted temperature, which is defined as

$$T_{SF} = \frac{\int_{P=1000_{mb}}^{P=0_{mb}} \bar{T}(P) \cdot SF(P)dP}{\int_{P=1000_{mb}}^{P=0_{mb}} SF(P)dP} \qquad (12)$$

where P = the pressure of the standard FNOC pressure levels
$\bar{T}$ = the mean temperature between levels, and
SF = the value of the signal function for each of the layers.

As noted earlier, the signal received has the inherent property of being integrated over altitude. In a similar manner, the T_{SF} is an average temperature, vertically weighted (by the signal function) over the depth of the atmosphere.

Determination of Calibrated Radiances

The upper branch in Figure 12 relates to the conversion of the digital electrical voltages recorded onboard the spacecraft to calibrated radiometric signals. This conversion was accomplished by using the previously discussed ground calibration data to establish the instrument responsivity and data

acquired during the space viewing periods to establish the instrument zero position.

To convert instrument voltages to radiance measurements, the detector output voltages V and ΔV or $\Delta V'$, the reference blackbody temperature TBB1, and the instrument mainframe temperature TBB2 are combined using the following equations:

$$L = \frac{(V-\beta)}{R^V} + L(BB1) \tag{13}$$

and

$$\Delta L = \frac{(\Delta V - \Delta V_{ref})}{R^{\Delta V}} \tag{14}$$

where R^V and $R^{\Delta V}$ are the respective responsivities (volts/watt cm^{-2} sr^{-1}) of the V and ΔV detector channels and are a function of the mainframe temperature TBB2,

ΔV_{ref} is the ΔV channel offset and is a function of mainframe temperature and the V channel voltage

β is the V channel offset voltage, and

L(BB1) is the radiance of the reference blackbody and is a function of its temperature TBB1.

Using the above relationships and the calibration data the radiometric signals were calculated at 1-second intervals over the 12-hour period between balance 4 and balance 5. The actual values of the calibration constants are given in Appendix 1.

Calculation of Regression Coefficients

As shown in the second branch of Figure 12, the first step in the calculation of the regression coefficient sets is the specification of an appropriate set of atmospheric models. Nine model atmospheres were

constructed to encompass the range of atmospheric conditions viewed by the MAPS OSTA-1 experiment. As depicted in Figure 13, the temperatures at the surface span the range from 280 K to 310 K; the lapse rate is constant with height, +6.5 K/km, following the 1976 U.S. Standard Atmosphere; and the tropopause heights increase and the tropopause temperatures decrease as the surface temperature increases. The tropopause heights and temperatures were chosen from those reported in the worldwide radiosonde data set of November 10-14, 1981. The appropriate seasonal and latitudinal distribution of the humidity profiles, tropopause heights, and temperatures were verified by comparing the constructed profiles with those reported in the literature [Makhover, 1972; Strand, 1973; Danielsen et al., 1980; Swanson and Trenberth, 1981; Newell et al., 1972; NASA, 1981].

The construction of the model atmospheres included the vertical distribution of five principal gas species in addition to the temperature profile. Three of the five, carbon monoxide, nitrous oxide (280 ppbv), and carbon dioxide (330 ppbv), are well mixed in the free troposphere. The single ozone profile used in the model atmospheres was determined from special ozonesondes launched from Wallops Island, Virginia [NASA, 1981] and from climatological records of ozone profiles [Danielsen et al., 1980]. The water vapor profile varied for each model in keeping with the seasonal and latitudinal characteristics of each atmospheric model.

The radiometric signals, L, ΔL, and $\Delta L'$, that would be received by the sensor for each of the model atmospheres were calculated by means of a line-by-line radiative transfer program. The atmospheres were divided into layers that corresponded to the FNOC analysis layers. The calculations were carried out over a wavelength range corresponding to the bandpass of the instrument, a surface temperature range from 268 K to 313 K, solar zenith

angles of 0° and 75°, surface emissivities of 0.98 and 0.88, and CO mixing ratios from 0 to 220 ppbv. For the ΔV and $\Delta V'$ channel calculations, CO was considered to be the only infrared active gas present. For the V channel calculations CO, H_2O, CO_2, O_3, and N_2O were considered in the calculations. Laboratory and aircraft flight tests have demonstrated that the gas filter discriminates against the interfering effects of gases with overlapping bands extremely well. In the broadband channel (V), their absorption effects must be considered, however. All lines were considered to be Lorentzian; line parameters were taken from Rothman [1981].

The sets of regression coefficients relating the measured radiometric signals to the carbon monoxide mixing ratios were determined on the basis of the previously performed theoretical calculations. The method employed was an extension of that described in Wallio et al. [1983]. Two 15-coefficient sets (a "coarse" set covering a mixing ratio range from 0-220 ppbv and a "fine" set covering a range from 20 to 137 ppbv) were generated for each model atmosphere and selected solar zenith angle-surface emissivity combinations. Each of these sets included the effects of the full range of surface temperature.

Meteorological and Terrain Data

The third branch of Figure 12 outlines the process by which the atmospheric and surface data required for the data reduction are processed. In the first step, the gridded FNOC northern and southern hemispheric analyses for 0 and 12 Z of November 14, 1981, were processed to produce T_{SF} values for each channel at each grid point. (Since the signal functions are different for the ΔV and $\Delta V'$ channels, the T_{SF} values are different for the two channels.) These gridded T_{SF} fields were combined with the spacecraft ephemeris data by linear spatial interpolation to produce a value of T_{SF} at

each point at which the instrument had acquired data. This was done for both the analysis that preceded and the analysis that followed the time of the data point. The T_{SF} values were then linearly interpolated in time between the analyses to produce values of T_{SF} appropriate to the latitude, longitude and time of each point at which CO data were acquired.

Great care was exercised in the spatial interpolation scheme when the ground track passed from one hemispheric projection to the other. As long as the sub-orbital point was located on the northern hemispheric projection, the interpolation was made using the values at the four nearest grid points from that analysis. (There are portions of the southern hemisphere included in the northern hemispheric projection.) If the sub-orbital point was located off the northern hemispheric projection, then the values at the four nearest grid points from the southern hemispheric projection were used to interpolate the T_{SF} value. When the edge of the analysis projection was reached, a 2-point interpolation was applied to the values of the two grid points nearest to the interpolation location. To smooth the edge effect, a 10-point running average was applied to all points within 1/2° north and south of the equator for each orbit as it crossed the equator.

Because, as discussed in the previous section, different sets of coefficients were used depending upon both the type of underlying surface and solar zenith angle, it was necessary that these be specified for each data point. The terrain data were generated using a Defense Mapping Agency 1° x 1° resolution terrain analysis provided by Dr. Richard Rapp [personal communication, 1983]. The solar zenith angle, θ, was calculated using normal methods.

CO Inference

The final inference of CO mixing ratio was carried out for all of the valid data points. First, the sets of regression coefficients for a particular data point were selected on the basis of the type of underlying surface and the solar zenith angle (θ). By using numerical simulations to study the effects of variable solar zenith angle and surface emissivity, it had been found that three combinations, when properly applied, would yield results having a r.m.s. error of less than 4% when applied to the range of conditions encountered during the flight. If the surface was water, the data were reduced assuming $\theta = 75°$ and $\varepsilon = 0.98$. If the surface was land and $\theta > 75°$, the data were reduced assuming $\theta = 75°$ and $\varepsilon = 0.98$. If the surface was land and $\theta < 75°$, the data were reduced assuming $\theta = 0°$ and $\varepsilon = 0.88$. It should be noted that the incorrect choice of coefficients might occur momentarily at a coastal crossing. This appears as a spike in the data. Since it is readily recognized in the data and since it always lasts less than 10 seconds, we have not included it in the error budget. Then the regression coefficient sets corresponding to the models having T_{SF} higher and lower than the T_{SF} of the data point were linearly interpolated on the basis of T_{SF} to yield a coefficient set appropriate to that particular data point. The measured radiometric signals for that data point were then put into the regression equations, and the equations were solved for the CO mixing ratio in each channel for both the "fine" and "coarse" coefficient sets. If the value fell within the range of the "fine" set, that CO value was used; otherwise, the value from the "coarse" set was used.

Cloud Filtering

Only CO data acquired when the field of view of the instrument is cloud free or when there are scattered low clouds (in the mixing layer) are valid.

Following the inference of the CO mixing ratio, it was necessary to reject those measurements that were contaminated by the presence of clouds. The effect of cloud (or of terrain of significant (> 1 km) height above sea level) is to cause erroneously high CO readings. The removal of cloud contaminated data was carried out in a stepwise manner. If the clouds were middle or high clouds, the effect was to produce extremely high CO values--on the order of a few hundred ppbv. These values were immediately excluded from the data set. The time-coded false-color infrared photographs were then examined in great detail, and they were compared to plots of CO mixing ratio versus time. By doing this it was possible to recognize data that were acquired through holes in broken cloud situations or to recognize the effect of isolated clouds in clear to partly cloudy conditions. The data were retained only if several seconds or more of data were acquired through the opening. The above two steps were all that was required in the northern hemisphere because the data there were all acquired under daylight conditions. In the southern hemisphere, the data were acquired under nighttime conditions, and it was not possible to use the photography. It had become clear during the processing of the data from the northern hemisphere, however, that the effects of clouds were recognizable in the plots of inferred CO versus time. The patterns were very distinct. The recognition of these patterns was used to remove the cloud contaminated data in the southern hemisphere. The results were checked against meteorological satellite imagery whenever possible. If any doubt existed, the data were rejected. After the above cloud filtering was complete, about 10,000 individual CO measurements remained for each channel. These are presented later in the paper.

Data Precision and Accuracy

The precision and accuracy of the MAPS experiment have been assessed in two ways. First, the impact of uncertainties that would affect the instrument output (calibration errors, instrument noise, and digitization errors, for example) have been studied, and errors that would arise from uncertainties in assumptions made or input data used in the data reduction scheme (for example, variation of surface emissivity or errors in the atmospheric temperature field) have been analyzed through the use of radiative transfer models. Second, the results of the experiment were compared within themselves and with independent, concurrent measurements of the CO mixing ratio.

Theoretical Prediction of Error

The accuracy of the experiment has been studied by examining potential error sources through the use of numerical models. These studies have dealt primarily with the ΔV channel of the instrument, and these will be discussed here. More limited studies of the $\Delta V'$ channel have produced results that are generally similar except that instrument-induced errors are somewhat larger in that channel because of its lower signal level. (The noise level is essentially the same in both channels.) Table 3 summarizes the results of these studies. The results shown in Table 3 were calculated for a mixing ratio of 55 ppbv, which is typical of the southern hemisphere. The studies were also carried out for a mixing ratio of 110 ppbv which would more nearly approximate a northern hemispheric value. As might be expected, the percentage error tends to decrease with increasing mixing ratio. Because the lower mixing ratio produces the larger percentage errors, we will discuss those results.

The instrument error of 12 percent includes the effect of detector noise, uncertainty in the measurement of internal blackbody and instrument mainframe temperatures, and digitization errors. Errors induced in the CO mixing

ratio by ΔV channel errors and by V channel errors were calculated separately and combined. A substantial portion of this 12-percent error results from detector noise. As a result, this error could be reduced by averaging the data over time. The 6-percent error attributed to the instrument is the result of the zero shift that was seen during the third space viewing period near the end of the data period.

The second major category of uncertainty is associated with errors introduced during the data inversion process. As Table 3 shows, the major potential sources of error here are related to uncertainty in the value in the mixing layer, in the water vapor profile, and in the temperature profile. A number of test cases were run in which T_{SF} values, calculated by spatial and temporal interpolation of the analyses, were compared to T_{SF} values calculated from radiosonde and aircraft derived temperature profiles that were acquired as part of the correlative measurements program for the experiment. These radiosonde and aircraft profiles were, of course, not part of the data set from which the analyses were derived. The largest difference resulted from a comparison with a temperature profile acquired by the NASA Convair 990 about 1000 km west of San Francisco, California. The descent took place in the vicinity of a rapidly developing intense storm. In this extreme case, the error in T_{SF} was 1.5 K.

If the errors shown in Table 3 are assumed to be independent, they can be combined by the root sum square method. This yields an overall accuracy estimate of about ±20 percent for the data acquired by the ΔV channel. Since some of the errors would tend to be systematic, it would be expected that the repeatability of the experiment should be somewhat better than that. Signal averaging would, of course, reduce the instrument noise component.

Experimental Assessment of Error

The precision and accuracy have been estimated by internal comparisons of the data and by comparing the results with independent measurements. Specifically, we have evaluated the precision of the shuttle experiment by comparing the inferred carbon monoxide mixing ratios for eight pairs of data points in each channel, with each pair representing a particular geographical location during two different passes of the satellite. In general, the comparisons were made between data taken at 1-1/2-hour intervals (1 orbit) although some comparisons were made between data taken at 3-hour intervals. To minimize the effect of very small-scale variations, the comparisons were made between 30-second averages of the data. This corresponds to a distance along the subsatellite track of 225 km. For the eight pairs of geographical locations, (three in the southern hemisphere and five in the northern hemisphere, all at latitudes greater than 33°), the magnitude of the differences in the paired readings was less than 3.1 percent for four pairs of high-pressure channel measurements and less than 6.2 percent for four pairs of the low-pressure channel measurements. Seven of the eight pairs of measurements disagreed by less than 8 percent in the high-pressure channel and 10 percent in the low-pressure channel. The rms difference for all eight pairs of measurements was 6.4 percent for the high-pressure channel and 8.9 percent for the low-pressure channel. Because the data were taken at different times and at somewhat different locations (generally within 250 km of each other), some atmospheric variability is reflected in the above numbers, although it is probably small.

The absolute accuracy of the data is more difficult to access. One set of direct aircraft-borne measurements was made in the vicinity of the data reported here. Aircraft flights were made during the mission at other

locations, but, unfortunately, they took place during periods when the satellite data were not reducible because of the spacecraft thermal control problems. Rasmussen et al. [1982] report CO measurements at latitudes between 30°S and 40°S and longitudes between 138°E and 149°E during the period of the STS-2 mission. They found the CO mixing ratio to be 66 ± 3ppbv in the altitude range from 1 to 4 km. If we assume that the atmosphere is uniformly mixed above 1 km (the approximate height of the mixing layer as reported by Rasmussen et al., 1982), we can compare our data to these measurements. The nearest satellite measurements occurred between latitudes 30°S and 35°S and longitudes 135°E to 140°E or just to the west of the area in which the direct measurements were made and 25°S to 30°S and 140°E to 145°E, or just to the north of the area in which the direct measurements were made. In the more southerly and westerly area (30°-35°S and 135°-140°E), the MAPS data have a value of 46 ppb in the higher pressure channel and 41 ppbv in the lower pressure channel. In the more northerly area (25°-30°S and 140°-145°E), the MAPS readings are 57 ppb in the higher pressure channel and 46 ppbv in the lower pressure channel. This experimental result supports the theoretical error assessment of ±20 percent, and it provides strong evidence that the actual error is in the negative direction. The lower pressure channel indicates a mixing ratio that is systematically 10 to 20 percent lower than the value indicated by the higher pressure channel.

To determine the degree of bias between the two channels, we have compared the measurements by forming zonal averages over 5° wide bands from 40°N to 40°S. If the atmosphere were uniformly mixed throughout the troposphere and lower stratosphere, the two channels should give the same reading. This condition is likely to be most closely approached at high southern latitudes. In view of that, the ratio of the measured values for the

two channels was calculated for the band 30-35°S where the ratio $(CO_{\Delta V'}/CO_{\Delta V})$ was 0.8458 and for the band 35-40°S where the ratio was 0.8465. The zonal averages for the low-pressure channel were then divided by 0.8461 (the average of 0.8458 and 0.8465). The results of these calculations are shown in Table 4. As can be seen from the last column of the table, the value of the quantity derived by dividing the measured mixing ratio of the low-pressure channel by 0.8461 is within ±3 percent of the measured CO value for the high-pressure channel over the latitude range from 25°N to 40°S. Over this latitude range one might expect the atmosphere to be uniformly mixed over the altitude range in which this experiment is sensitive. This is either because the tropopause is high (in the tropics) or because the tropospheric mixing ratio is near the stratospheric value (at southern midlatitudes). On the basis of the foregoing, it appears that the two channels are largely redundant (as would be expected from the signal functions) over much of the atmosphere, and that there is about a 15-percent bias of unknown cause between the two channels, with the low-pressure channel being biased low relative to the high-pressure channel. Thus it appears that within each channel, data variations larger than 10 percent between different locations are real, but that the absolute values may be about 20-percent low in the high-pressure channel and 30-percent low in the low-pressure channel as compared to a set of direct measurements. These errors are approximately of the order of those predicted by the theoretical analyses for the ΔV channel.

Discussion of Results

Regional Aspects and Discrimination of Detail

Figures 14(a) through (g) show all of the usable CO data acquired by the MAPS experiment during the useful 12-hour portion of the flight of the STS-2. As an example, we will discuss the data from orbit 31 as shown in Figure

14(g). The data are shown for the two channels beginning when the spacecraft crossed the equator west of South America, moving in a northeasterly direction, and ending when it maneuvered out of data-taking attitude east of Australia. In all, there are just over 1900 data points for each channel during orbit 31; they were acquired over a period of about 66 minutes.

In general, the shapes of the curves for the two channels are similar, although the data from the low-pressure ($\Delta V'$) channel are biased lower than the data from the high-pressure (ΔV) channel. It can be seen that there are regions of total cloud cover, for example near 50°W, 20°W, 10°E, and 145°E, where the data are not recoverable; regions that are cloud-free or with only low, scattered clouds, for example from 30°E to 80°E where essentially all of the data are recovered; and regions of broken clouds where a small percentage of the data are retained, for example the equatorial regions around 80°W and 90°E. In these regions of broken clouds, the data appear to be somewhat noisy. This noise is the effect of very small, low clouds passing through the field-of-view. The actual noise level of the instrument system is best illustrated by the data taken over Saudi Arabia where the noise level is about 5 ppbv peak-to-peak. These data, taken over land, include effects of variable surface emissivity, but over Saudi Arabia this variation is small.

The data are, in general, highly structured. Variations in the CO mixing ratio are found as a function of both latitude and longitude. The CO mixing ratio is higher in the equatorial region near 80°W (about 90 ppbv in the high-pressure channel) than it is in the equatorial region near 80°E (about 55-60 ppbv). It can also be seen that the mixing ratio increased as the spacecraft moved in a nearly west to east direction between 15°W and 5°E. Over the central Atlantic, the mixing ratio rises, then falls again. The gradients between 20°N and 33°N are about 1 ppbv per 100 km along the track or

2.2 ppbv per degree of latitude. This is somewhat higher than those reported by Seiler and Fishman [1981] for these latitudes, but is similar to the gradients that they reported for eastern North America between 30°N and 40°N. Since their data were acquired on the east coast during the summer while our data were acquired over the central Atlantic in the fall, we would not expect the data from the two sets to be directly comparable. The gradients reported here are also somewhat lower than those calculated from Reichle and Condon (1979) for the latitudes between 25°N and 35°N, but again, those data were acquired on the east coast during the winter rather than the fall. A particularly intriguing feature in the data is the 7- to 8-ppbv decrease in the mixing ratio seen in the high-pressure channel over Saudi Arabia. Careful examination of the subsatellite photography shows no apparent change in the texture or color of the underlying surface and it also shows a complete absence of clouds. Since the instrument was stable during this very short period of about 6 minutes, there is no reason to believe that the feature is not real. All indications are that the free tropospheric CO mixing ratio did decrease by about 15 percent over the Saudi Arabian desert as compared to the surrounding region.

As the spacecraft crossed the equator southbound near 80°E, the mixing ratio rose steadily in a region of partial cloudiness and achieved a maximum near 20°S, fell rapidly until the west coast of Australia was reached near 23°S, and then began to increase sharply. This fall and subsequent rise occurred under essentially clear sky conditions. East of 120°E and south of 28°S, the sky was cloud covered with only a few holes large enough to allow valid data to be reduced. These few data did indicate, however, that the mixing ratio was essentially constant over southeastern Australia at a value that was significantly lower than the value over central western Australia.

Summary

The MAPS experiment which flew as part of the OSTA-1 payload aboard the space shuttle on November 12-14, 1981, has demonstrated the ability of a spaceborne remote sensor to measure the volume mixing ratios of carbon monoxide at the few tens of parts per billion level in the middle and upper troposphere. The carbon monoxide distribution in the altitude range between 3 and 12 km has been determined between 38°N latitude and 38°S latitude over all longitudes with a precision of about 10 percent. The MAPS measurements were found to be within 20 to 30% of near simultaneous aircraft measurements made over Australia.

As might be expected, lower mixing ratios were found in the southern hemisphere, with the lowest readings (about 40 ppbv) being found south of 20°S over the eastern Pacific Ocean and South America. Highest values (> 100 ppbv) were found in a band between 15°N and 5°S that extended from just west of South America eastward to at least central Africa, but that did not extend as far east (at these latitudes, at least) as the Indian Ocean south of India. The second highest group of readings was found over southeastern China and the adjacent ocean areas. These high values appeared to spread eastward as far as the central Pacific Ocean. Somewhat enhanced mixing ratios were found in the vicinity of the eastern Mediterranean Sea and over the eastern North Atlantic Ocean. Because the experiment is not very sensitive to gas in the mixing layer, there must be some mechanism, e.g. thunderstorms, that rapidly transports the CO to the middle and upper troposphere from its surface or mixing layer source. The MAPS data show that the carbon monoxide mixing ratio in the middle and upper troposphere not only is a function of latitude, but also is a strong function of longitude.

References

Abel, P. G., P. J. Ellis, J. T. Houghton, G. Peckham, C. D. Rodgers, S. D. Smith and E. J. Williamson, The selective chopper radiometer for Nimbus D, Proc. Roy. Soc., London A-320, 35 1970.

Acton, L. L., M. Griggs, H. D. Hall, C. B. Ludwig, W. Malkmus, W. D. Hesketh, and H. G. Reichle, Jr., Remote measurement of carbon monoxide by a gas filter correlation instrument, AIAA Journal, 11, 899-900, 1973.

Danielsen, E. F., R. S. Hipskind, and S. E. Gaines: High resolution vertical profiles of wind, temperature, and humidity obtained by computer processing and digital filtering of radiosonde and radar tracking data from the ITCZ experiment of 1977, NASA CR 3269, Contract NAS2-10023, April 1980, p. 115.

Dianov-Klikov, V. I., V. V. Lukshin, I. Ya. Sklyarenko, and Yu. P. Shakula, The variations of carbon monoxide content throughout the entire thickness of the earth's atmosphere, Isv. Atmospheric and Ocean Physics, 11, 320-324, 1975.

Doherty, G. M., R. E. Newell, and H. G. Reichle, Jr., Analysis of remote measurements of tropospheric carbon monoxide concentrations made during the 1979 Summer Monsoon Experiment (MONEX), submitted to the J. of Geophys. Res.

Heidt, L. E., J. P. Krasnec, R. A. Lueb, W. H. Pollock, B. B. Henry, and P. J. Cruzen, Latitudinal distributions of CO and CH_4 over the Pacific, J. Geophys. Res., 85 7329, 1980.

Hesketh, W. D., H. G. Reichle, Jr., W. A. Massey, T. V. Ward, H. H. Zwick, A gas filter correlation instrument for atmospheric trace constituent monitoring, in Remote Sensing of Earth Resources, edited by V. F. Shahrakhi, University of Tennessee Space Institute, Tullahoma, pp. 527-556, 1977.

Lamontagne, R. A., J. W. Swinnerton, and V. J. Linnenbom, Non-equilibrium of carbon monoxide and methane at the air-sea surface, J. Geophys. Res., 76, 5117, 1971.

Logan, J. A., J. Prather, S. C. Wofsy, M. B. McElroy, Tropospheric chemistry: A global perspective, J. Geophys. Res., 86. 7210, 1981.

Ludwig, C. B., M. Griggs, W. Malkmus, and E. R. Bartle, Measurement of air pollutants from satellites. 1: Feasibility considerations, Applied Optics, 13, 1494-1509, 1974.

Makhover, Z. M., Altitude and temperature of tropopause over the northern hemisphere, Meteorologiya i Gidrologiya, 7, 28-35, 1972.

NASA, Wallops International Publication WFC 1032.1-81-113 Field Measurement Support Office Data Supporting the MAPS Experiment (Measurement of Air Pollution from Satellites) Flown Aboard STS-2 as part of the OSTA-1 Payload, Nov. 12-15, 1981, December 15, 1981.

Newell, R. E., and D. J. Gauntner, Experimental evidence of inter-hemispheric transport from airborne carbon monoxide measurements, J. Appl Meteor., 18, 696, 1979.

Newell, R., J. Kidson, D. Vincent, and G. Boer, General Circulation of Tropical Atmosphere and Interactions with Extratropical Cyclones, Vol. 1, MIT press, 1972.

Newell, R. E., E. P. Condon, and H. G. Reichle, Jr., Measurements of CO and CH_4 in the troposphere over Saudi Arabia, India, and the Arabian Sea, during the 1979 International Summer Monsoon Experiment (MONEX). J. Geophys. Res., 86, 933, 1981.

Rasmussen, R. A., M. A. K. Khalil, and A. J. Crawford, Natural and anthropogenic trace gases in the southern hemisphere, Geophys. Res. Lett., 9, 704-707, 1982.

Reichle, H. G., Jr., and E. P. Condon, Vertical profiles of CO and CH_4 in the lower and middle troposphere over the eastern United States January 1978, Geophys. Res. Lett. 6, 1979.

Reichle, H. G. Jr., S. M. Beck, R. E. Haynes, W. D. Hesketh, J. A. Holland, W. D. Hypes, H. D. Orr, III, R. T. Sherrill, H. A. Wallio, J. C. Casas, M. S. Saylor, and B. B. Gormsen, Carbon monoxide measurements in the troposphere, Science, 218, 1024, 1982.

Reichle, H. G. Jr., H. A. Wallio, J. C. Casas, and E. P. Condon, The Gas Filter Radiometer for Carbon Monoxide Measurements During the 1979 Summer Monsoon Experiment (MONEX), submitted to the J. of Geophys. Res.

Robinson, E., and Robbins, R. C., Evaluation of carbon monoxide data obtained on Eltanin Cruises 27, 29, and 31, Antarctic J. of the U.S., 3, 194, 1968.

Rothman, L. S., AFGL atmospheric absorption line parameters compilations: 1980 version, Applied Optics, 20, 1981.

Seiler, W., The cycle of atmospheric CO, Tellus, XXVI, 116-135, 1974.

Seiler, W., and J. Fishman, The distribution of carbon monoxide and ozone in the free troposphere, J. Geophys. Res., 86, 7255, 1981.

Seiler, W., and C. Junge, Carbon monoxide in the atmosphere, J. Geophys. Res., 75, 2217, 1970.

Seiler, W., and P. Warneck, Decrease of carbon monoxide mixing ratio at the tropopause, J. Geophys. Res., 77, 3204, 1972.

Settle, M., and J. V. Taranik, Use of the space shuttle for remote sensing research: Recent results and future prospects, Science, 218, 993, 1982.

Shaw, J. H, The abundance of atmospheric carbon monoxide over Columbus, Ohio, Astrophysical Journal, 128, 428-440, 1958.

Strand, O. N., Expected accuracy of tropopause height and temperature as derived from satellite radiation measurements, NOAA Technical Report ERL 295-WPL28, p. 73, December 1973.

Swanson, G. S. and K. E. Trenberth, Interannual variability in the southern hemisphere tropopause, Monthly Weather Review, 109, 1890-1897, 1981.

Swinnerton, J. W., and R. A. Lamontagne, Carbon monoxide in the South Pacific Ocean, Tellus, 26, 136, 1974.

Wallio, H. A., J. C. Casas, B. B. Gormsen, H. G. Reichle, Jr., and M. S. Saylor, Carbon monoxide mixing ratio inference from gas filter radiometer data, Applied Optics, 21, 749-754, 1983.

Ward, T. V., and H. H. Zwick, Gas cell correlation spectrometer: GASPEC, Applied Optics, 14, 2896-2904, 1975.

Figure Captions

Figure 1. Schematic diagram of a gas filter radiometer.

Figure 2. Normalized MAPS signal functions for 110 ppbv carbon monoxide.

Figure 3. Electro-optical layout of the instrument.

Figure 4. Photograph of the instrument showing the various subassemblies.

Figure 5(a). Typical V channel calibration curve. Negative values imply that the scene is colder than the reference blackbody.

(b). V channel responsivity as a function of instrument temperature

(c). V channel offset as a function of instrument temperature

Figure 6(a). Typical ΔV channel calibration curve.

(b). ΔV channel responsivity as a function of instrument temperature

(c). ΔV channel zero reference singal as a function of instrument temperature

Figure 7(a). Typcial $\Delta V'$ channel calibration curve.

(b). $\Delta V'$ channel responsivity as a function of instrument temperature

(c). $\Delta V'$ channel zero reference signal as a function of instrument temperature

Figure 8. ΔV channel output while viewing deep space

Figure 9. $\Delta V'$ channel output while viewing deep space

Figure 10. ΔV zero reference level during flight

Figure 11. $\Delta V'$ zero reference level during flight

Figure 12. Procedure for the inferral of carbon monoxide mixing ratios.

Figure 13. Atmospheric models used in the data reduction.

Figure 14. Carbon monoxide mixing ratios measured by the MAPS experiment.

(a) Orbit 24, November 14, 1981, GMT 318:01:18:44 to 318:02:48:18

(b) Orbit 26, November 14, 1981, GMT 318:04:17:53 to 318:05:47:27

(c) Orbit 27, November 14, 1981, GMT 318:05:47:27 to 318:07:17:01

(d) Orbit 28, November 14, 1981, GMT 318:07:17:01 to 318:08:46:35

(e) Orbit 29, November 14, 1981, GMT 318:08:46:35 to 318:10:16:09

(f) Orbit 30, November 14, 1981, GMT 318:10:16:09 to 318:11:45:43

(g) Orbit 31, November 14, 1981, GMT 318:11:45:43 to 318:13:15:16

TABLE 1. OSTA-1/MAPS Instrument Characteristics

Detected gas	Carbon monoxide
Spectral band	2080 to 2220 cm^{-1}
Detector type	PbSe, cooled to 195 K
FOV	4.33°
Entrance aperture	2.94 cm x 2.94 cm
Bandwidth	0.14 Hz

Gas cell pressure	CO	He	N_2
Cell 1 $\Delta V'$	76 torr	2 torr	0 torr
Cell 2 ΔV	266 torr	2 torr	0 torr
Cell 3 Vacuum	0 torr	76 torr	0 torr
Calibrate	140 torr	2 torr	550 torr

NEL V	1.7×10^{-7} watts $\cdot$ cm^{-2} $\cdot$ sr^{-1}
ΔV, $\Delta V'$	5.7×10^{-9} watts $\cdot$ cm^{-2} $\cdot$ sr^{-1}
Size	.90 x .76 x .56 meters
Mass	84 kg
Power, average in vacuum	73 watts
Temperature range (baseplate)	273 K to 288 K
Data rate	1 sample set (40 bits per second)
Data storage	107 hours maximum
Camera	35 mm, aerial, 1 photo every 23 seconds when surface of Earth illuminated
Film	Aerochrome 2443 false color infrared

TABLE 2. Test Conditions for Postflight Instrument Characterization Tests

Instrument Temperature (Kelvins)	Secondary Standard Target Temperature (Kelvins)	Secondary Standard Reference Cell Gas Mixtures (Percent CO by Volume)
272.66	273.16*	2.5
276.66	280.16**	3.8
282.16	293.16	10.9
289.16	305.16	
	312.16	
	320.16**	

*Target temperature used in calibration of V channel only.

**Target temperature equivalent to MAPS inflight calibration blackbody temperatures.

TABLE 3. Theoretical Error Estimate for MAPS Experiment at CO Mixing Ratio of 55 ppbv

Error Source	Magnitude of Perturbation	Error in CO (Percent)
Instrument		
Noise & Temperature Uncertainties		12
Bias Shift		6
Atmospheric Models		
Lorentz/Voigt		0.5
Layering		0.5
H_2O	25 to 90 Percent Relative Humidity	8
O_3	± 20 Percent of Nominal	2
Mixing Layer	1/2 to 2X of Uniform Mixed Value	8
N_2O Mixing Ratio	280 vs. 305 ppbv	0.3
Date Inversion		
Regression		4
Solar Zenith Angle and Emissivity		4
Atmospheric Temperature	±2 K	8
Root Sum Squared Estimate of Combined Error		± 20

TABLE 4. Zonal Average CO for High and Low Pressure Channels

Latitude Band	High Press. CO	Low Press. CO	Low Press. CO / 0.8461	(Low Press. CO / 0.8461) / High Press. CO
40°N-35°N	58.28	44.52	52.62	0.903
35°N-30°N	63.29	49.87	58.94	0.931
30°N-25°N	61.82	49.81	58.87	0.952
25°N-20°N	59.53	49.47	58.47	0.982
20°N-15°N	63.28	52.99	62.62	0.990
15°N-10°N	64.33	53.49	63.22	0.983
10°N- 5°N	70.59	58.02	68.57	0.971
5°N- 0	69.92	58.18	68.76	0.983
0 - 5°S	62.20	52.43	61.97	0.996
5°S-10°S	55.52	45.83	54.17	0.976
10°S-15°S	59.83	50.09	59.20	0.990
15°S-20°S	59.25	48.49	57.31	0.967
20°S-25°S	56.38	48.60	57.44	1.019
25°S-30°S	50.05	43.19	51.04	1.020
30°S-35°S	48.80	41.27	48.78	1.000
35°S-40°S	50.43	42.69	50.45	1.000

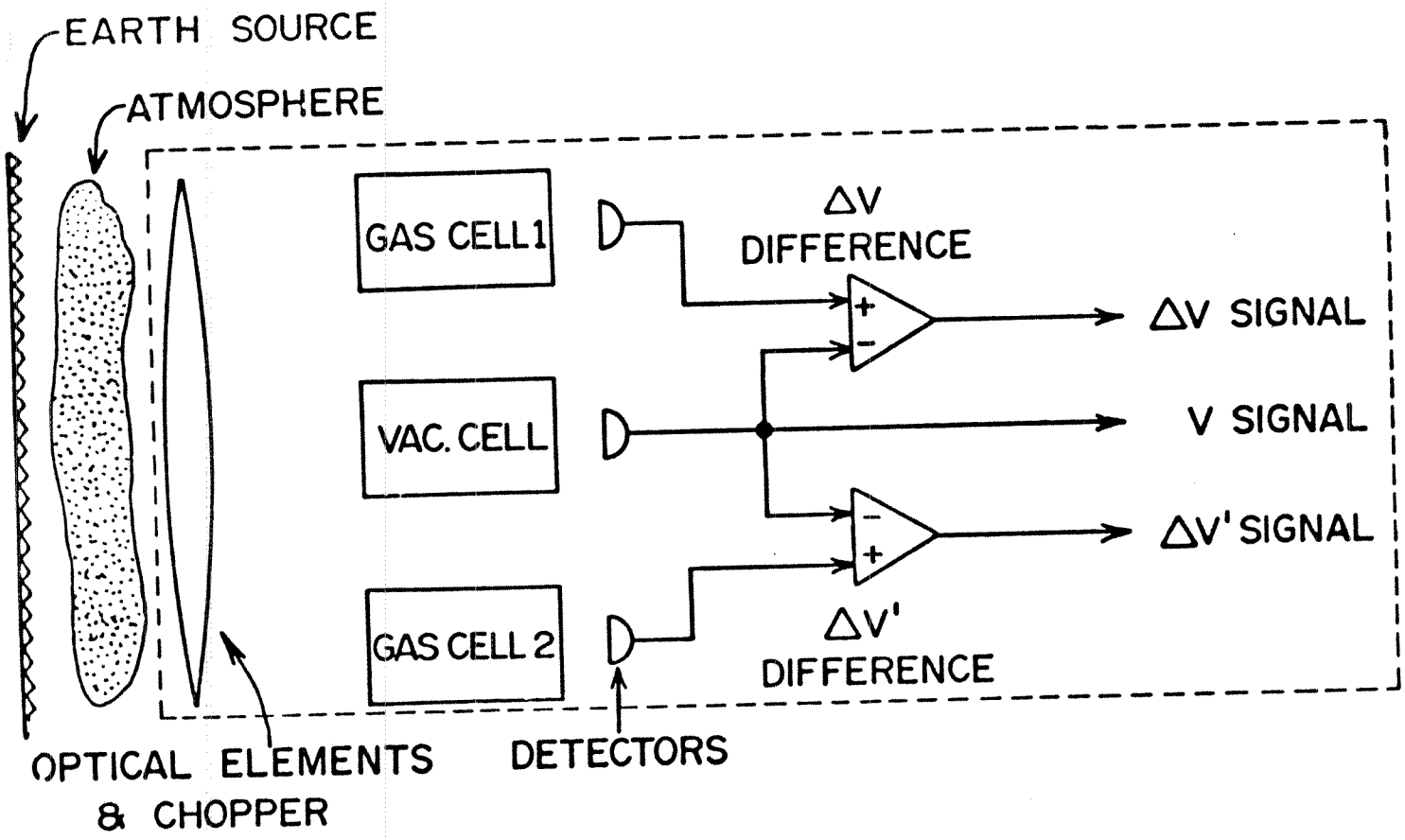
EARTH SOURCE
ATMOSPHERE
GAS CELL 1
VAC. CELL
GAS CELL 2
ΔV DIFFERENCE
ΔV' DIFFERENCE
ΔV SIGNAL
V SIGNAL
ΔV' SIGNAL
OPTICAL ELEMENTS & CHOPPER
DETECTORS

FIGURE 1

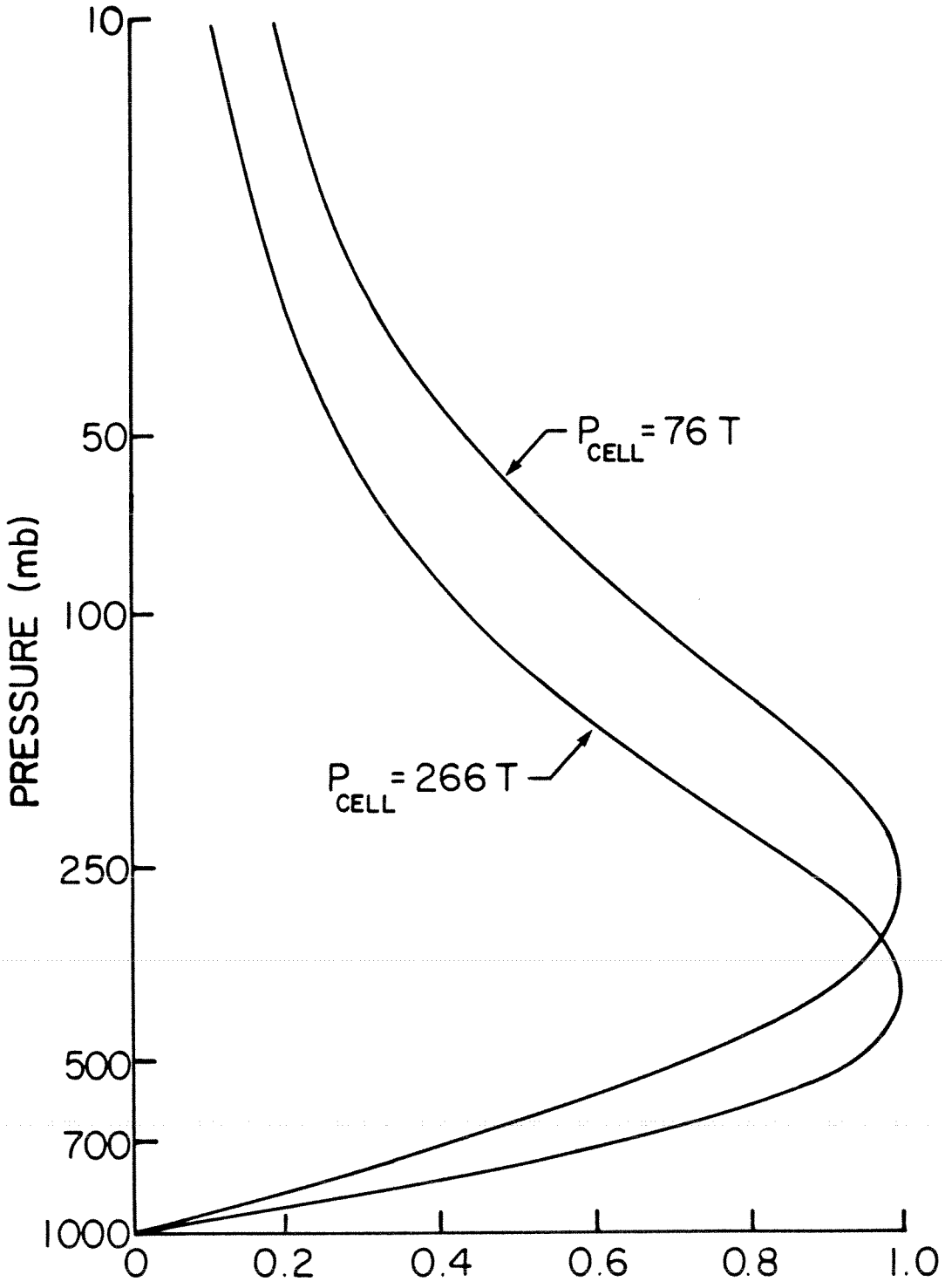
10
50
100
250
500
700
1000
PRESSURE (mb)
P_{CELL} = 76 T
P_{CELL} = 266 T
0
0.2
0.4
0.6
0.8
1.0

Figure 2

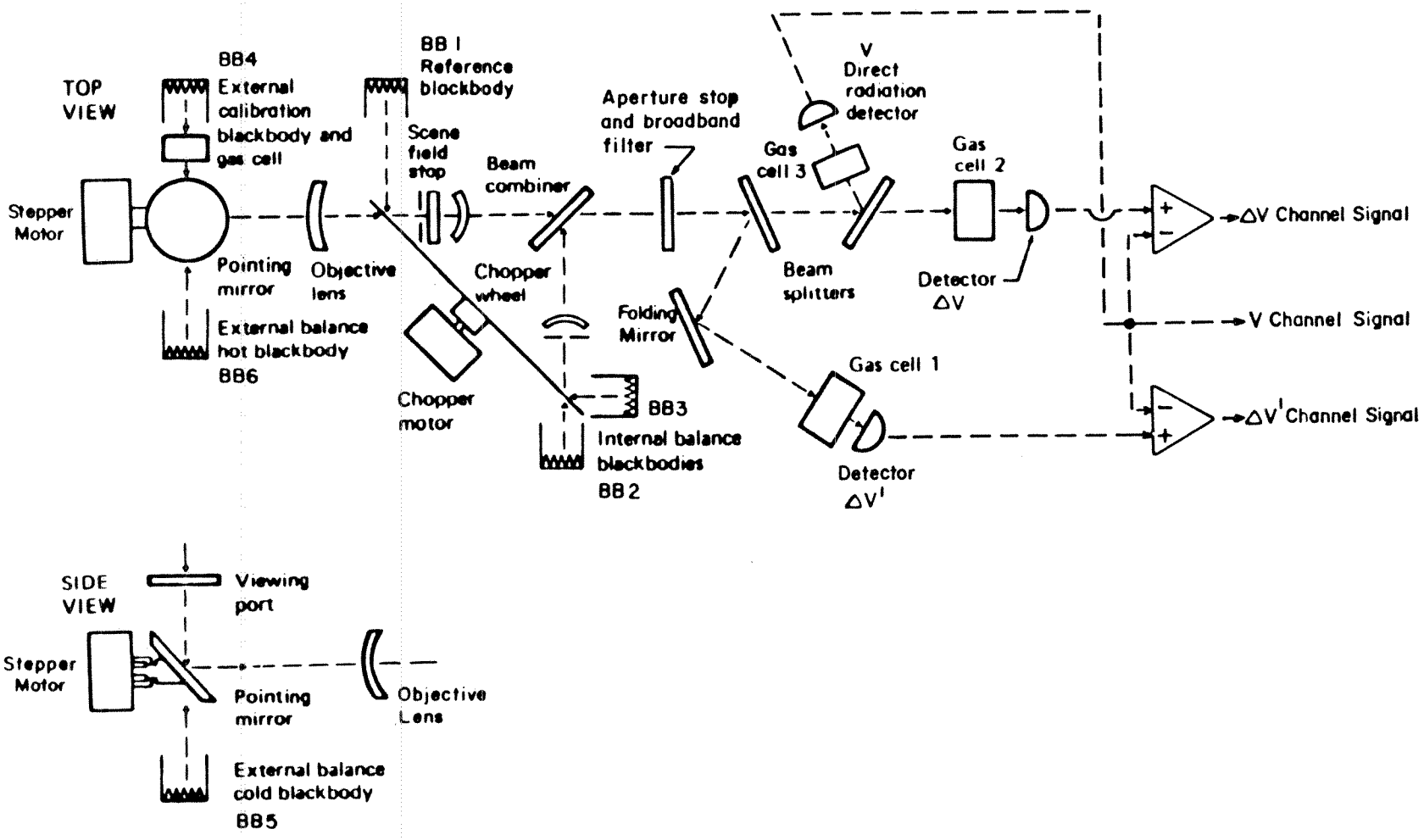
TOP
VIEW
BB4
External
calibration
blackbody and
gas cell
BB 1
Reference
blackbody
Scene
field
stop
Beam
combiner
Aperture stop
and broadband
filter
V
Direct
radiation
detector
Gas
cell 3
Gas
cell 2
Stepper
Motor
Pointing
mirror
Objective
lens
Chopper
wheel
Beam
splitters
Detector
ΔV
ΔV Channel Signal
V Channel Signal
External balance
hot blackbody
BB6
Folding
Mirror
Gas cell 1
Chopper
motor
BB3
Internal balance
blackbodies
BB2
Detector
ΔV'
ΔV' Channel Signal
SIDE
VIEW
Viewing
port
Stepper
Motor
Pointing
mirror
Objective
Lens
External balance
cold blackbody
BB5

Figure 3

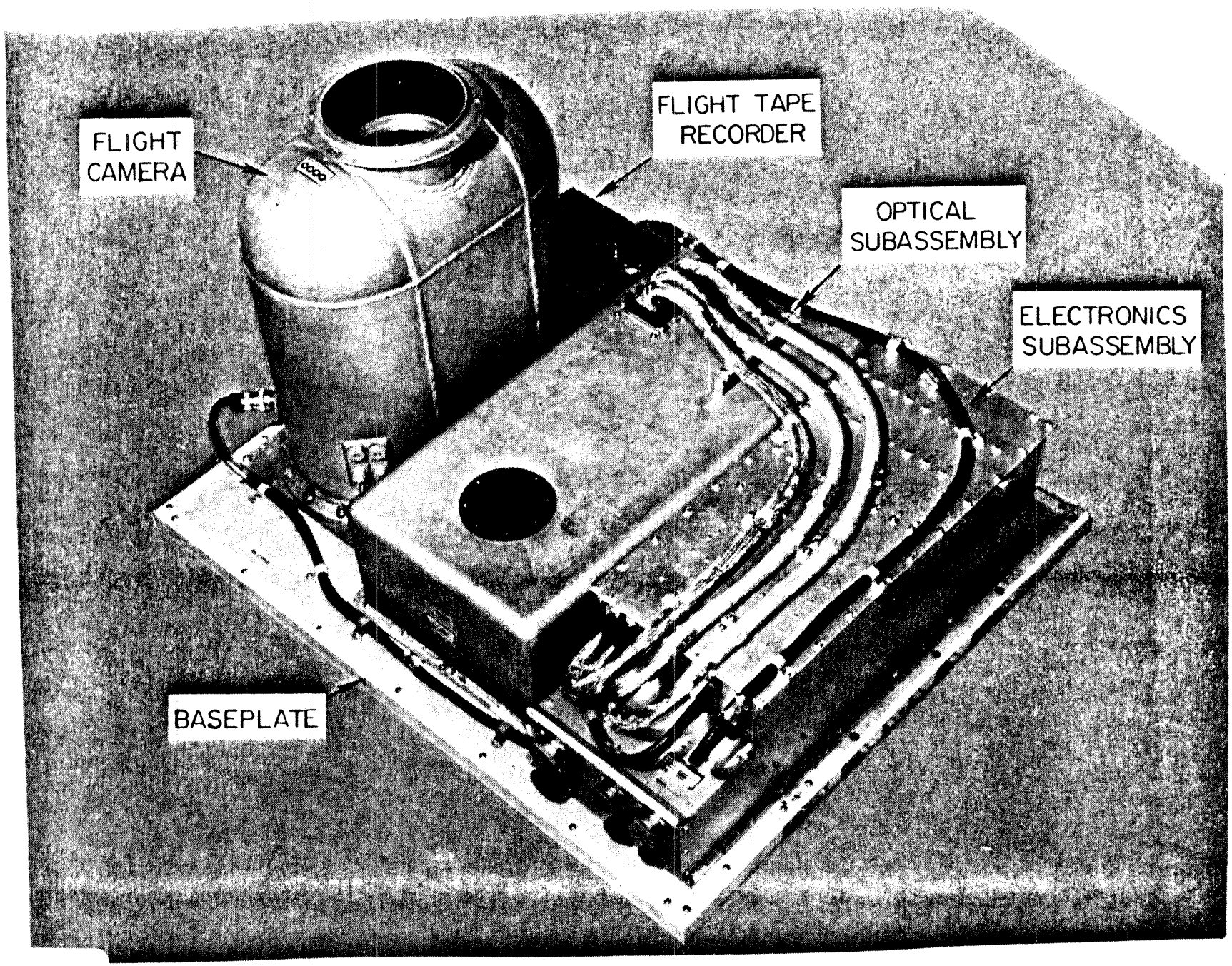
FLIGHT CAMERA
FLIGHT TAPE RECORDER
OPTICAL SUBASSEMBLY
ELECTRONICS SUBASSEMBLY
BASEPLATE

Figure 4

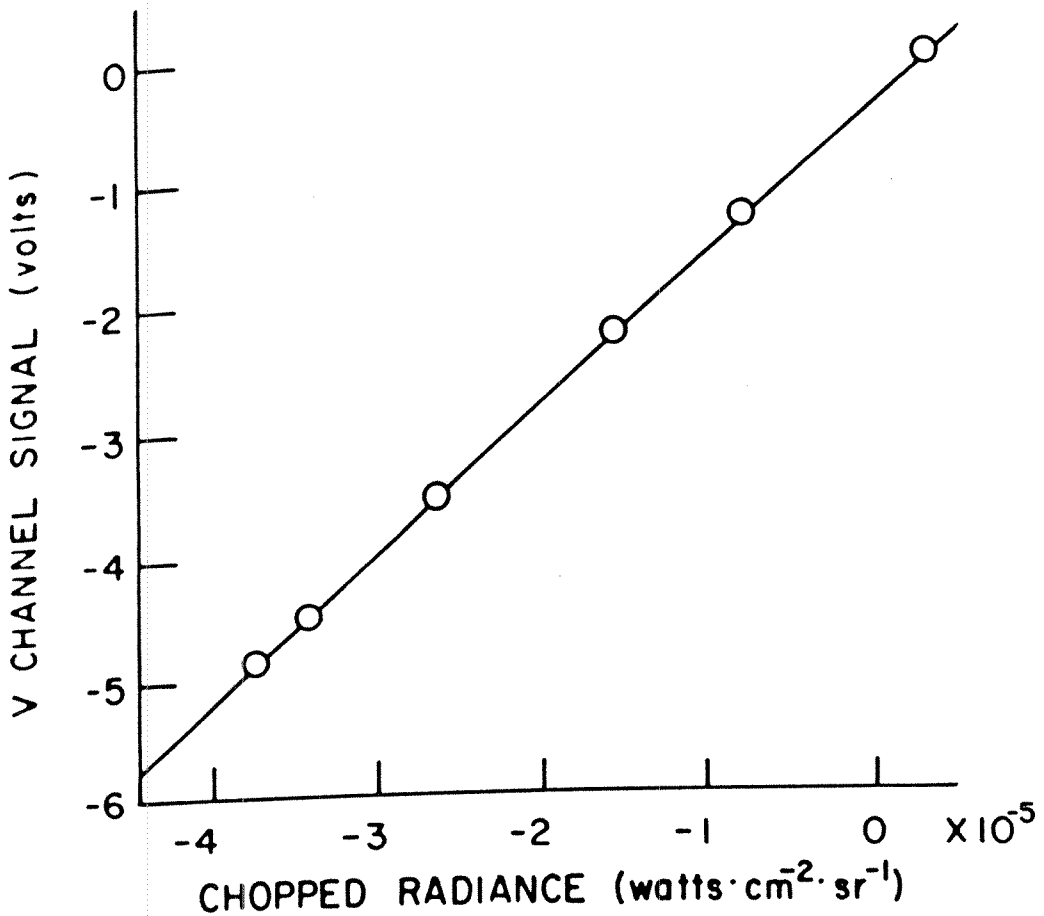
V CHANNEL SIGNAL (volts)
0
-1
-2
-3
-4
-5
-6
-4
-3
-2
-1
0
X 10⁻⁵
CHOPPED RADIANCE (watts·cm⁻²·sr⁻¹)

Figure 5(a)

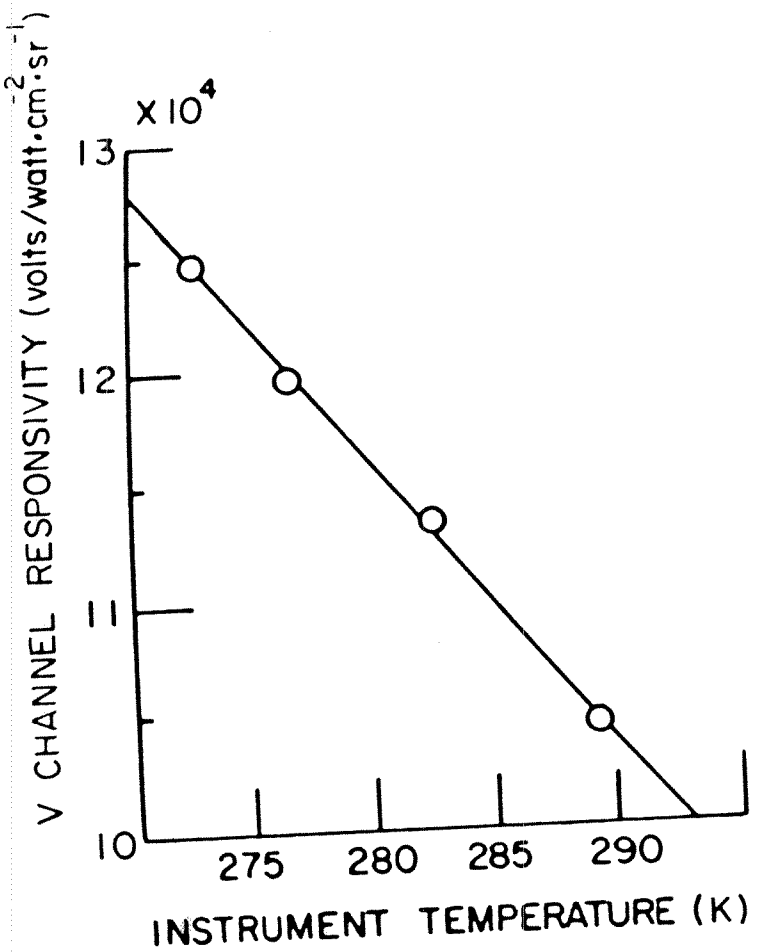
V CHANNEL RESPONSIVITY (volts/watt·cm⁻²·sr⁻¹)
X 10⁴
13
12
11
10
275
280
285
290
INSTRUMENT TEMPERATURE (K)

Figure 5(b)

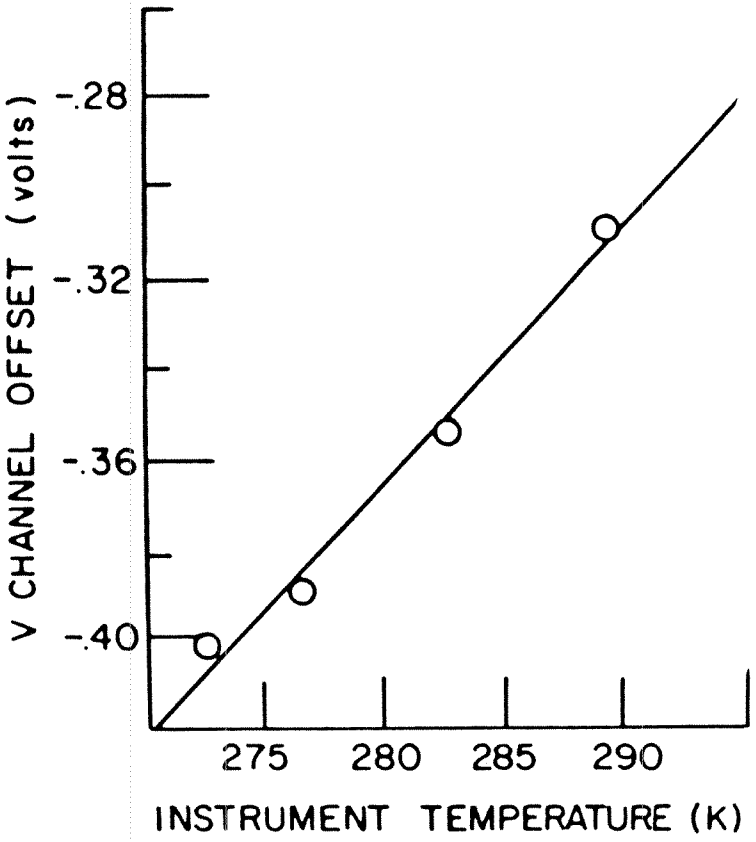
V CHANNEL OFFSET (volts)
-.28
-.32
-.36
-.40
275
280
285
290
INSTRUMENT TEMPERATURE (K)

Figure 5(c)

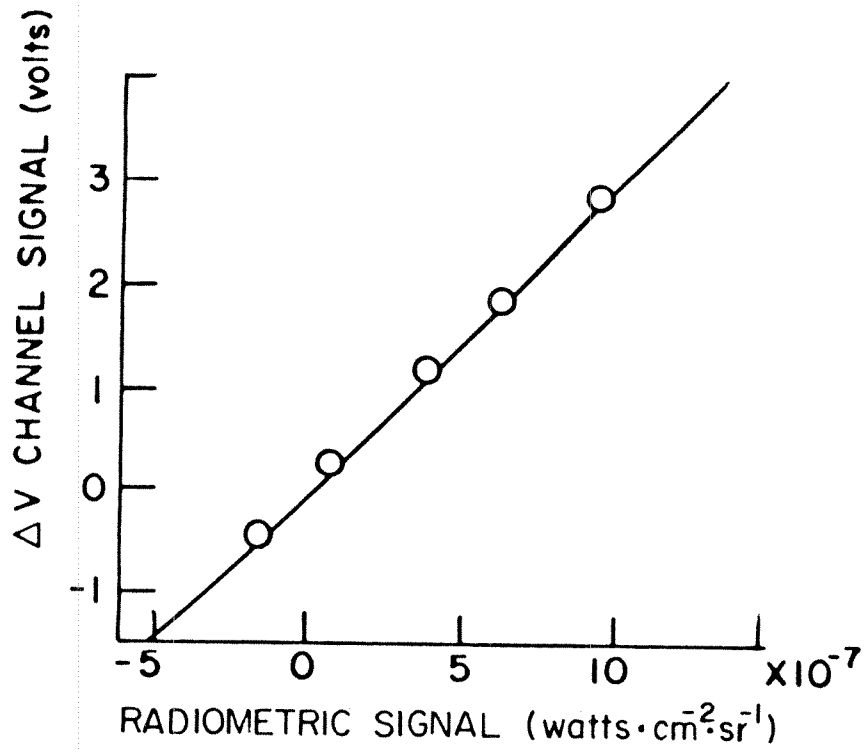
ΔV CHANNEL SIGNAL (volts)
3
2
1
0
-1
-5
0
5
10
X10⁻⁷
RADIOMETRIC SIGNAL (watts·cm⁻²·sr⁻¹)

Figure 6(a)

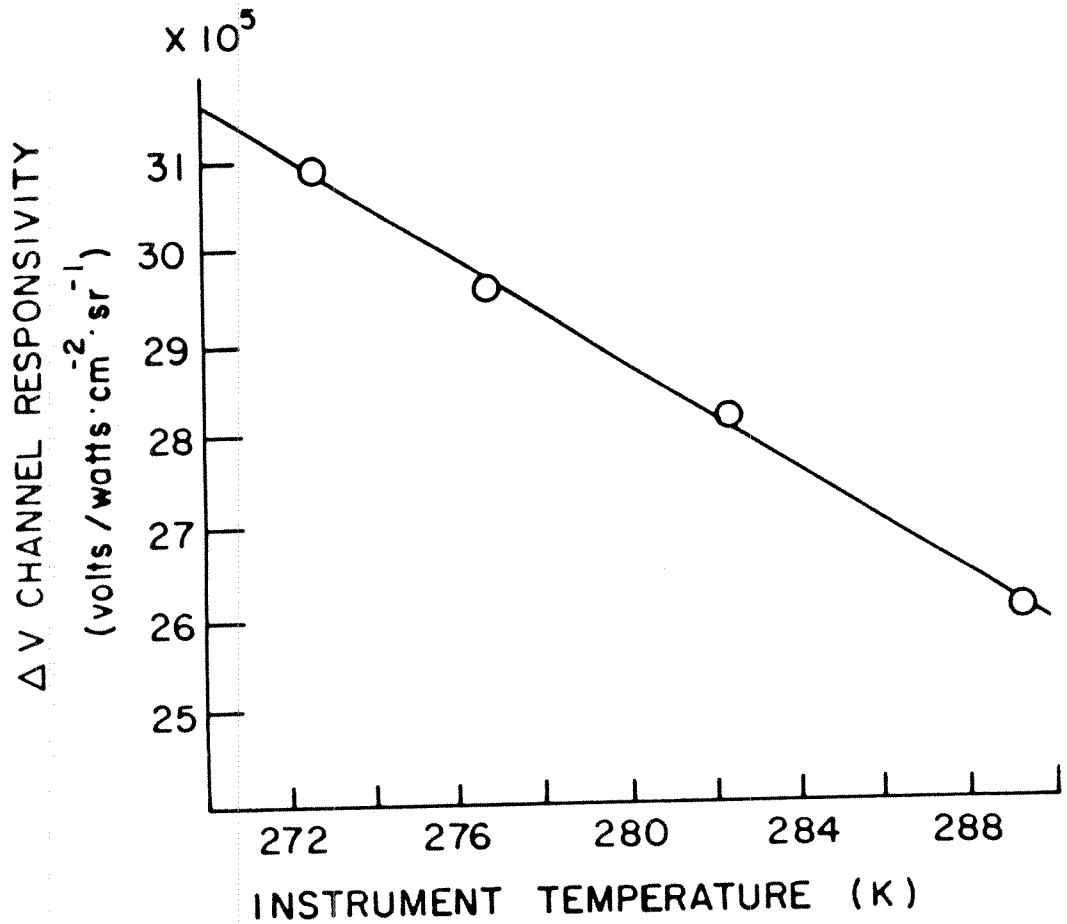
X 10^5
31
30
29
28
27
26
25
ΔV CHANNEL RESPONSIVITY
(volts / watts · cm^-2 · sr^-1)
272
276
280
284
288
INSTRUMENT TEMPERATURE (K)

Figure 6(b)

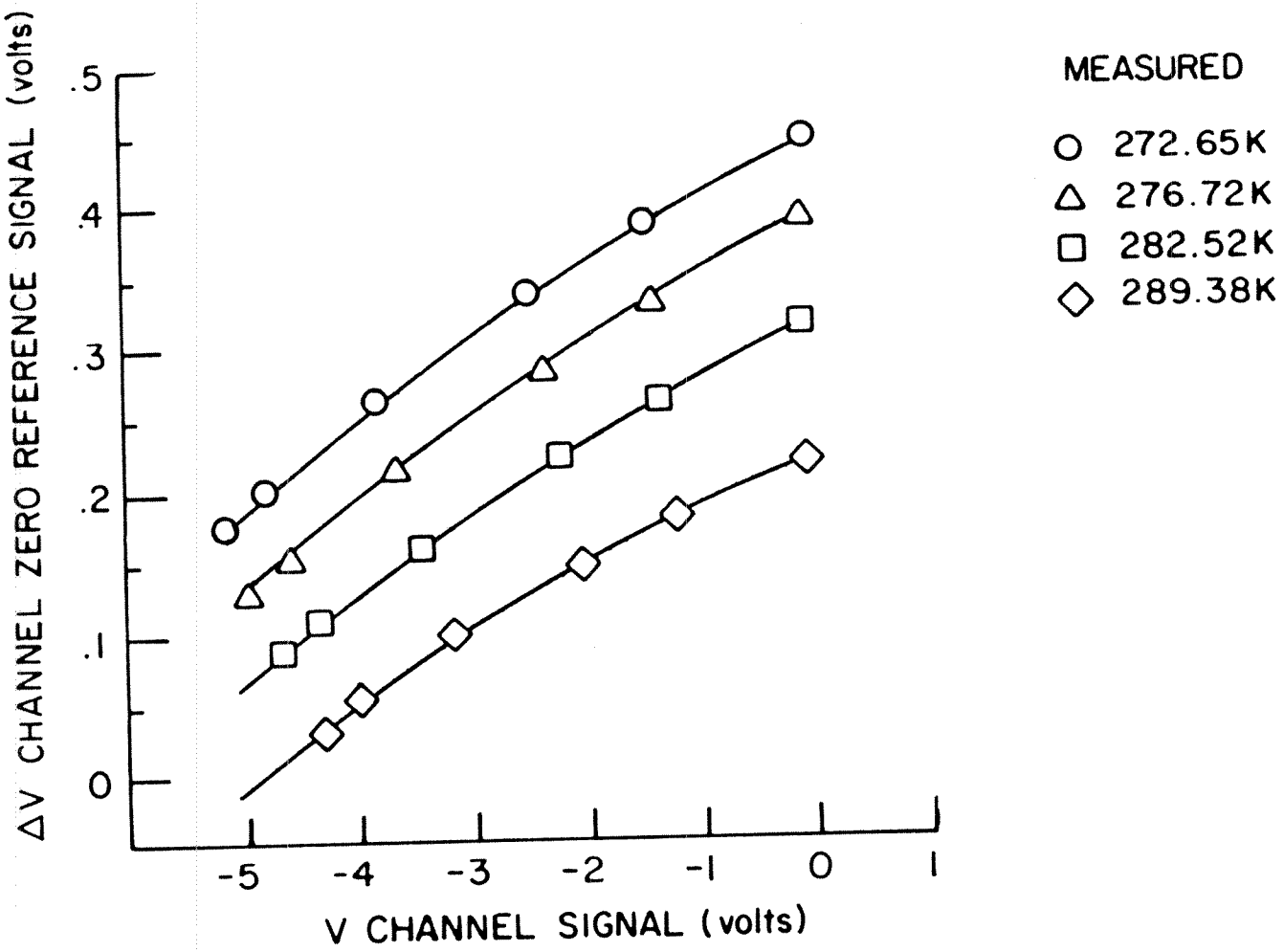
ΔV CHANNEL ZERO REFERENCE SIGNAL (volts)
.5
.4
.3
.2
.1
0
-5
-4
-3
-2
-1
0
1
V CHANNEL SIGNAL (volts)
MEASURED
272.65K
276.72K
282.52K
289.38K

Figure 6(c)

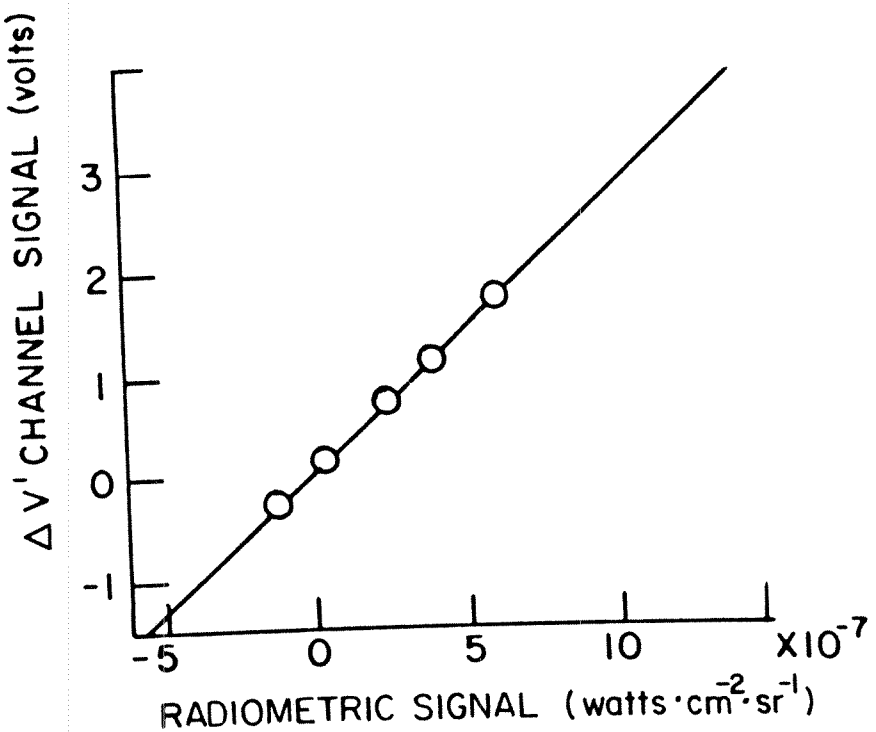
ΔV' CHANNEL SIGNAL (volts)
3
2
1
0
-1
-5
0
5
10
X10⁻⁷
RADIOMETRIC SIGNAL (watts·cm⁻²·sr⁻¹)

Figure 7(a)

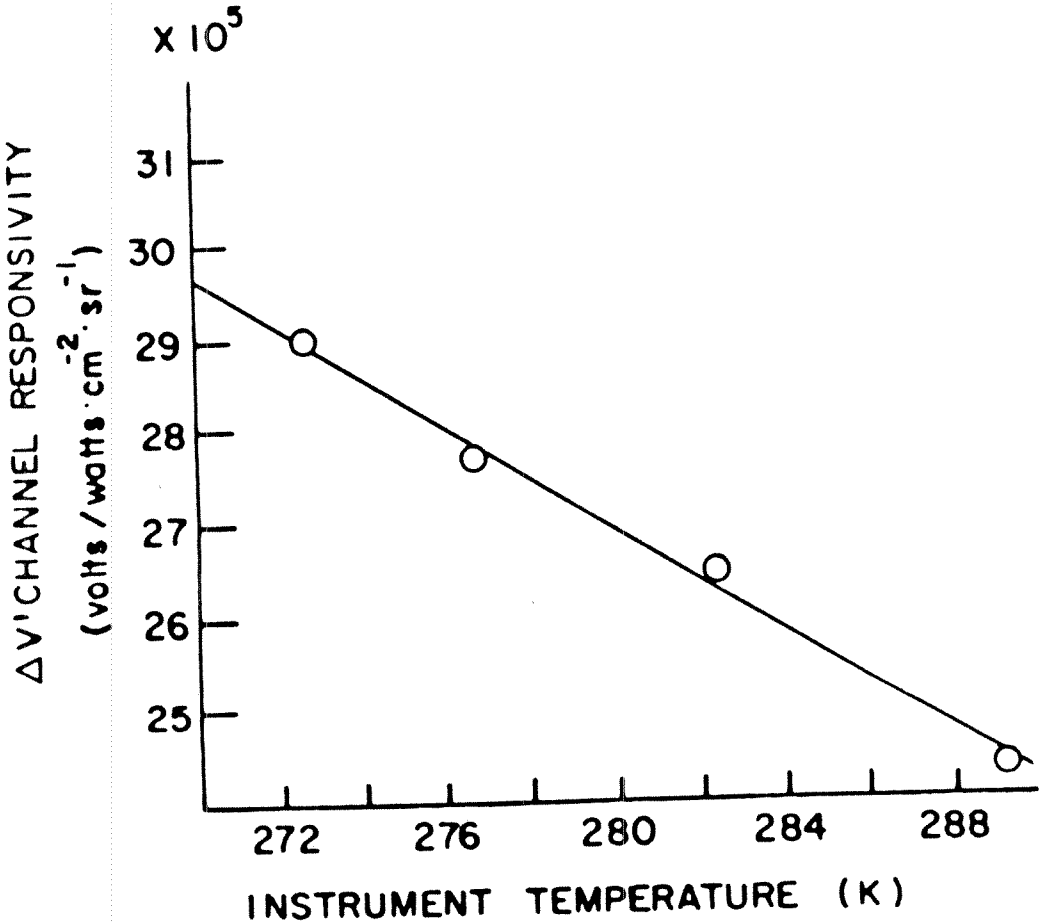
X 10^5
ΔV'CHANNEL RESPONSIVITY
(volts / watts · cm^-2 · sr^-1)
31
30
29
28
27
26
25
272
276
280
284
288
INSTRUMENT TEMPERATURE (K)

Figure 7(b)

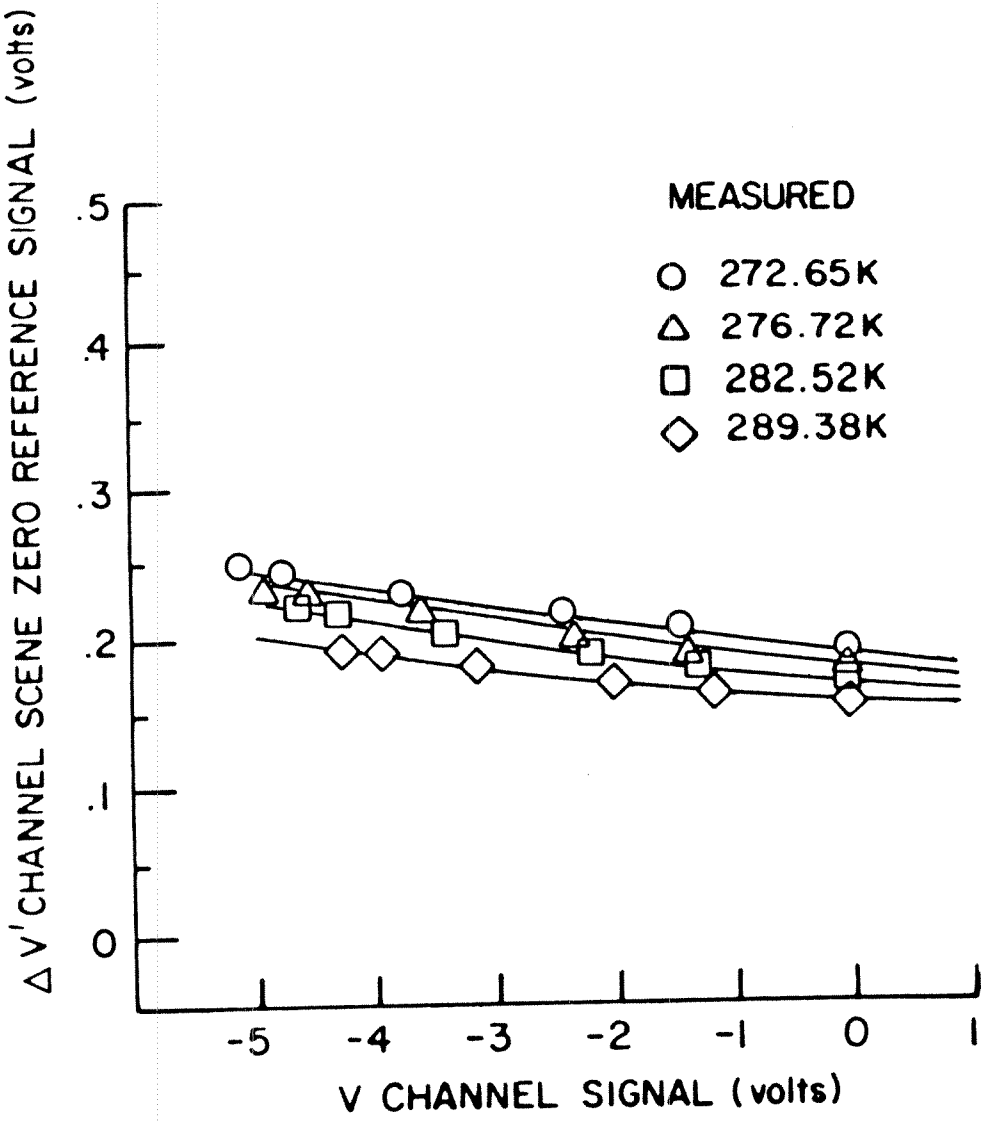
MEASURED
272.65K
276.72K
282.52K
289.38K
ΔV' CHANNEL SCENE ZERO REFERENCE SIGNAL (volts)
.5
.4
.3
.2
.1
0
-5
-4
-3
-2
-1
0
1
V CHANNEL SIGNAL (volts)

Figure 7(c)

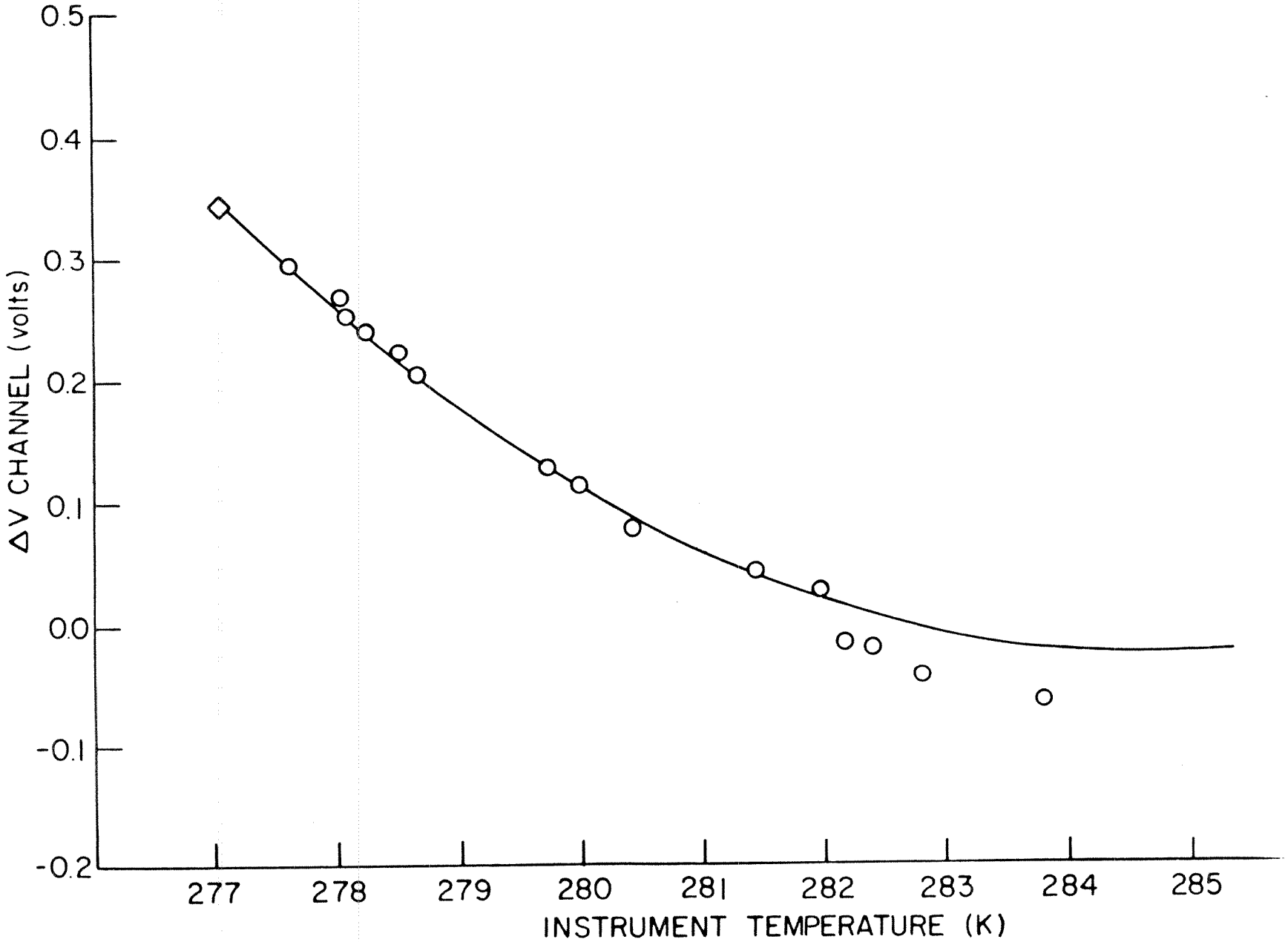
0.5
0.4
0.3
0.2
0.1
0.0
-0.1
-0.2
ΔV CHANNEL (volts)
277
278
279
280
281
282
283
284
285
INSTRUMENT TEMPERATURE (K)

Figure 8

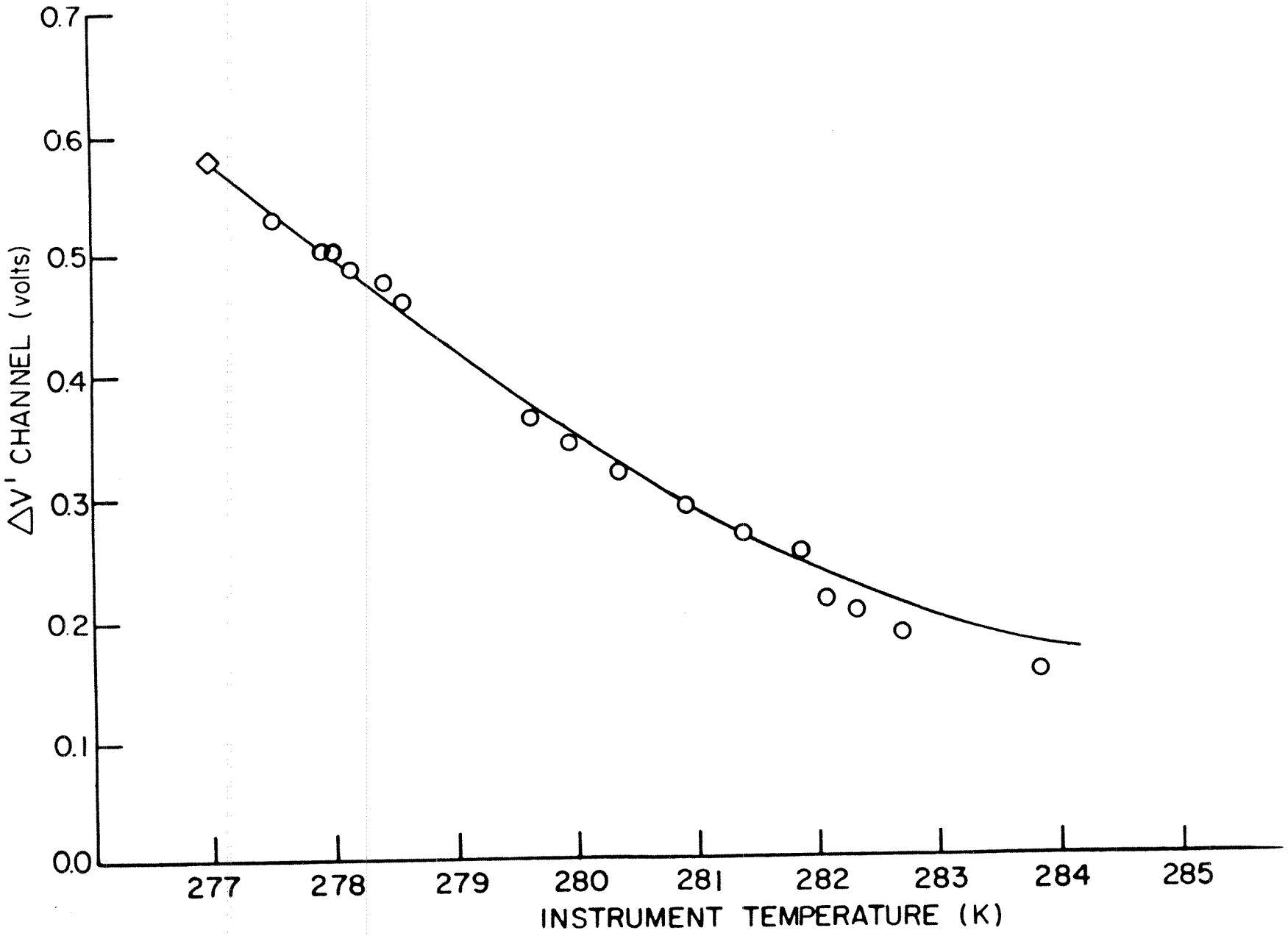
0.7
0.6
0.5
0.4
0.3
0.2
0.1
0.0
ΔV' CHANNEL (volts)
277
278
279
280
281
282
283
284
285
INSTRUMENT TEMPERATURE (K)

Figure 9

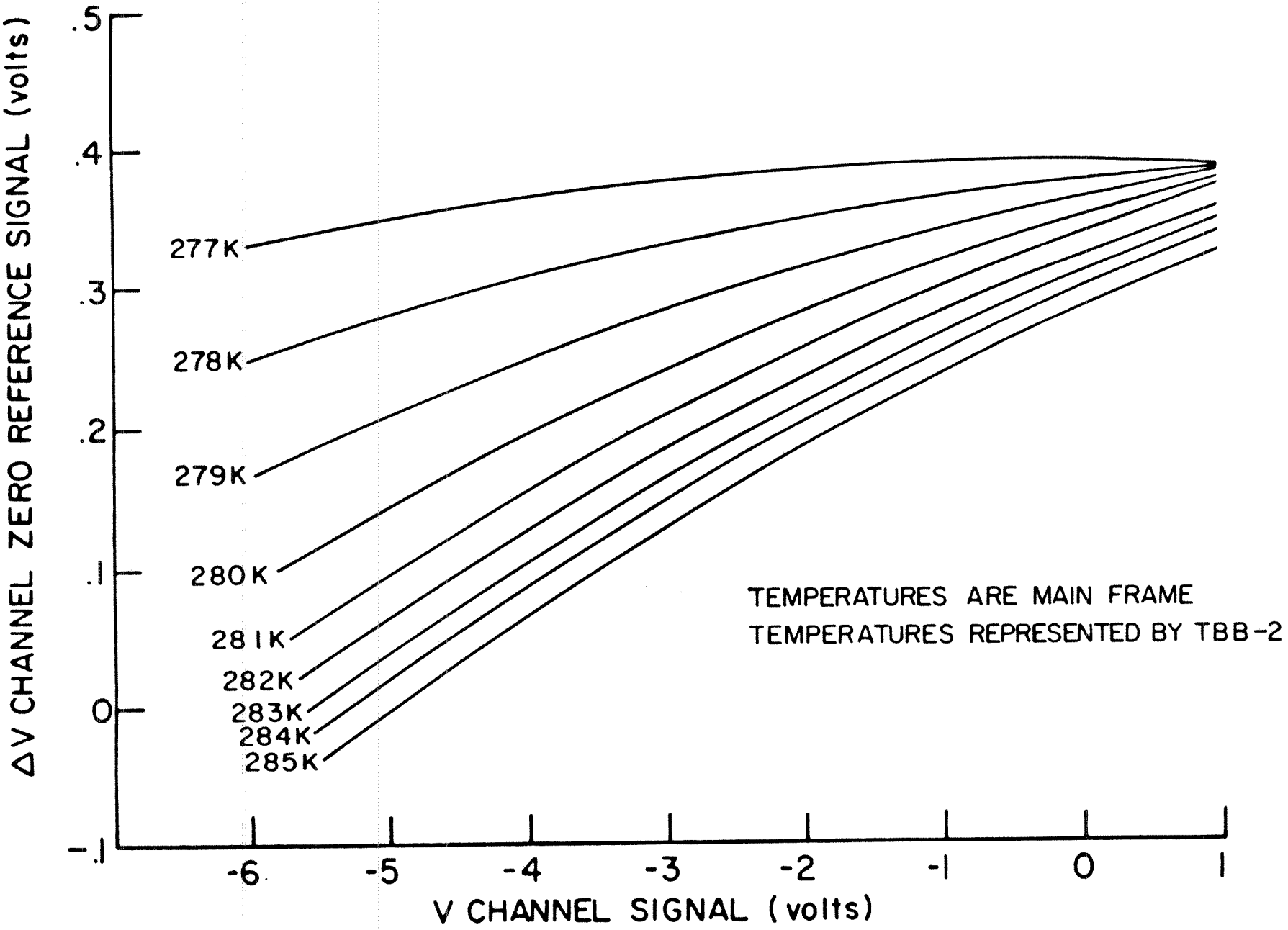
ΔV CHANNEL ZERO REFERENCE SIGNAL (volts)
.5
.4
.3
.2
.1
0
-.1
277K
278K
279K
280K
281K
282K
283K
284K
285K
TEMPERATURES ARE MAIN FRAME
TEMPERATURES REPRESENTED BY TBB-2
-6
-5
-4
-3
-2
-1
0
1
V CHANNEL SIGNAL (volts)

Figure 10

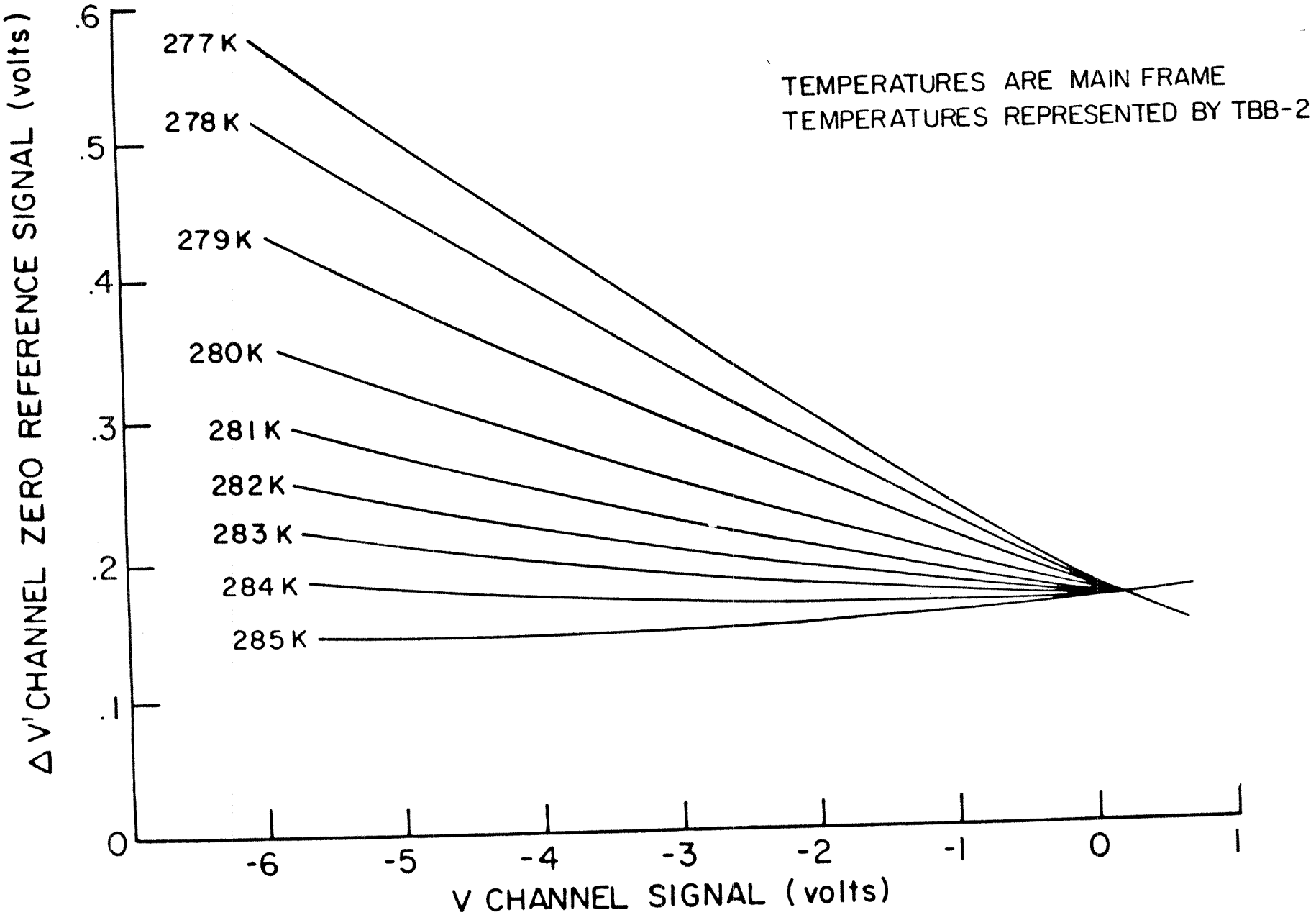
TEMPERATURES ARE MAIN FRAME
TEMPERATURES REPRESENTED BY TBB-2
277 K
278 K
279 K
280 K
281 K
282 K
283 K
284 K
285 K
ΔV' CHANNEL ZERO REFERENCE SIGNAL (volts)
.6
.5
.4
.3
.2
.1
0
-6
-5
-4
-3
-2
-1
0
1
V CHANNEL SIGNAL (volts)

Figure 11

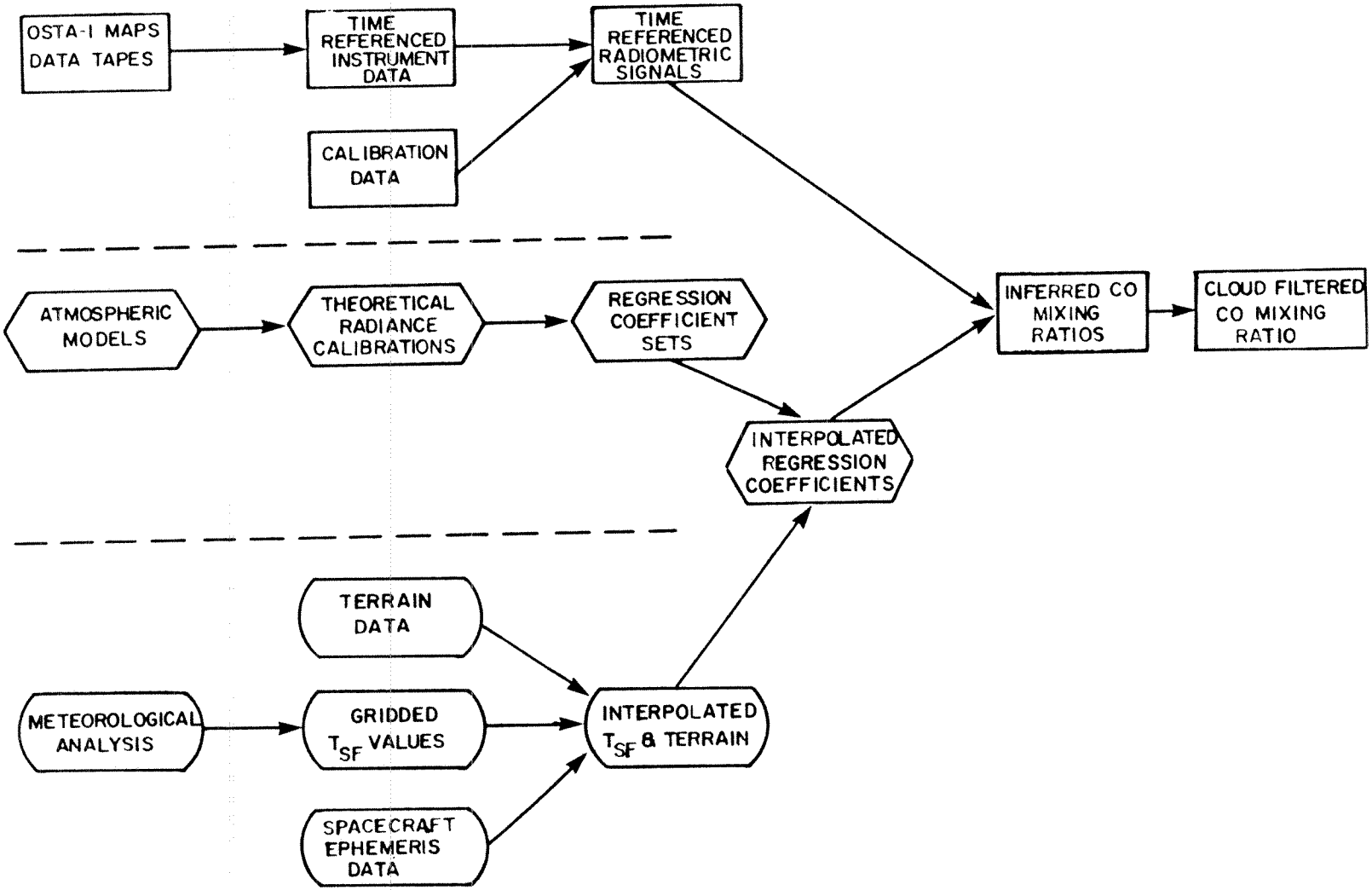
OSTA-I MAPS DATA TAPES
TIME REFERENCED INSTRUMENT DATA
TIME REFERENCED RADIOMETRIC SIGNALS
CALIBRATION DATA
ATMOSPHERIC MODELS
THEORETICAL RADIANCE CALIBRATIONS
REGRESSION COEFFICIENT SETS
INFERRED CO MIXING RATIOS
CLOUD FILTERED CO MIXING RATIO
INTERPOLATED REGRESSION COEFFICIENTS
TERRAIN DATA
METEOROLOGICAL ANALYSIS
GRIDDED T_{SF} VALUES
INTERPOLATED T_{SF} & TERRAIN
SPACECRAFT EPHEMERIS DATA

Figure 12

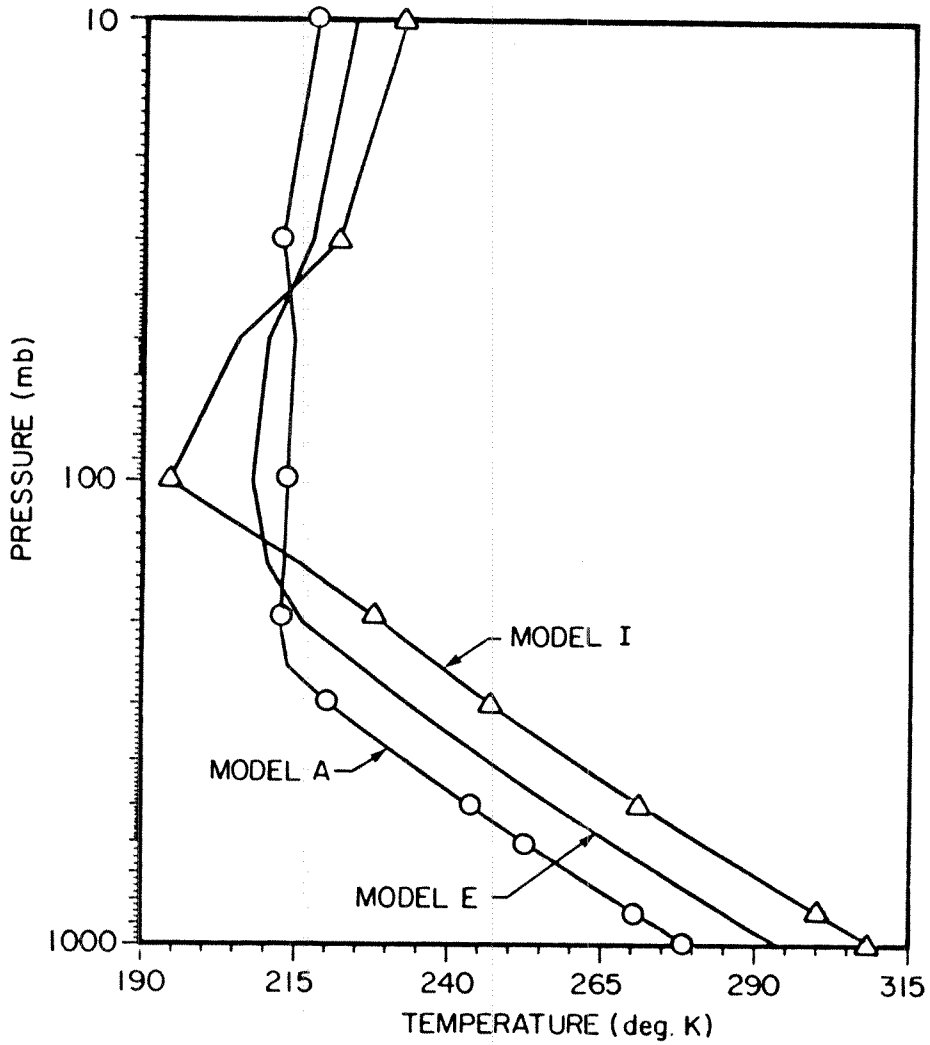

MODEL	SURFACE TEMPERATURE (°K)	TROPOPAUSE TEMPERATURE (°K)	TROPOPAUSE HEIGHT (km)
A	280	215	10.2
B	282.5	215	10.3
C	285	215	10.4
D	290	213	13.8
E	295	210	13.8
F	299	204	16.5
G	302.5	200	16.8
H	306	200	17.1
I	310	190	17.5

Figure 13

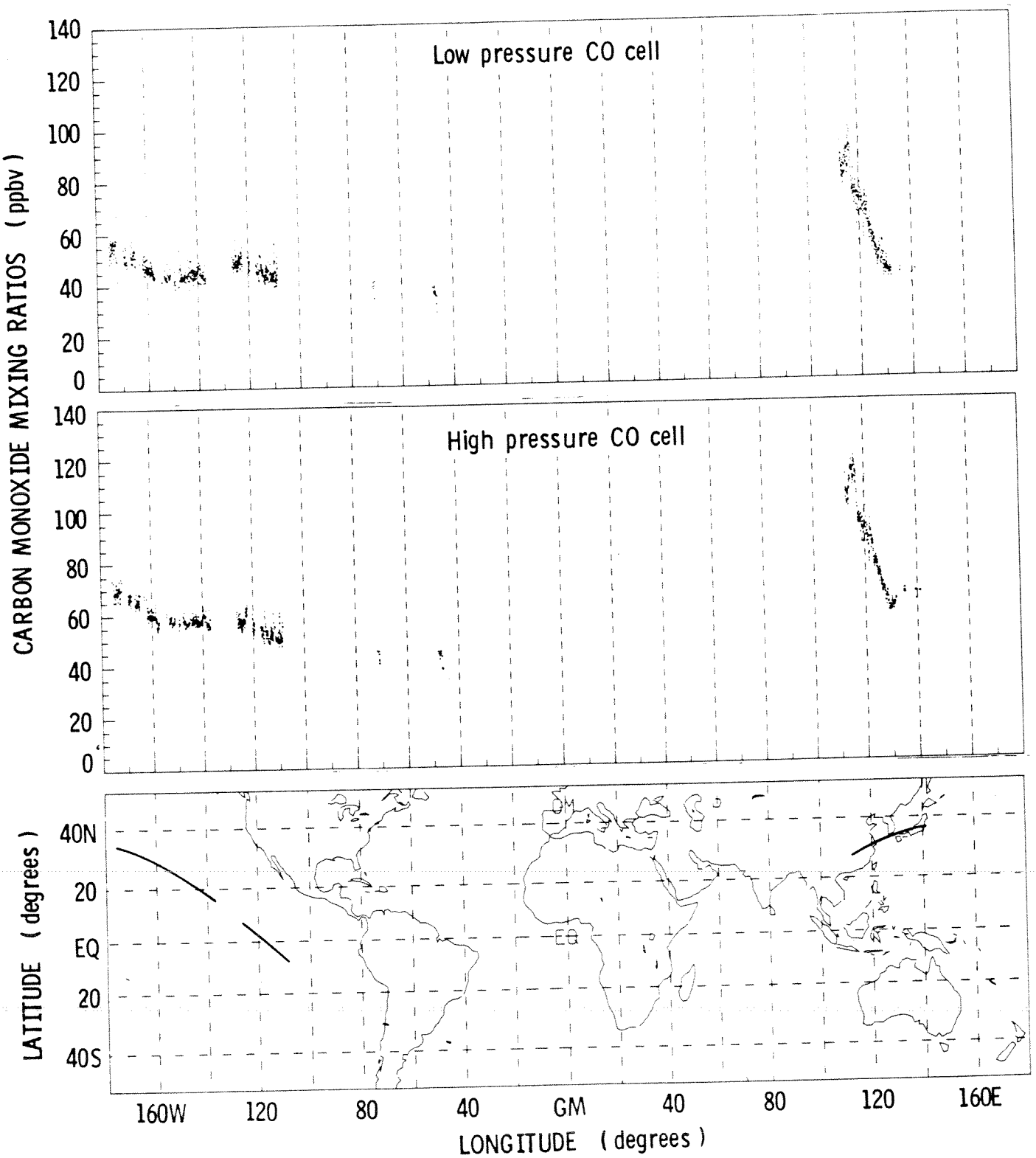
Low pressure CO cell
High pressure CO cell
CARBON MONOXIDE MIXING RATIOS (ppbv)
140
120
100
80
60
40
20
0
LATITUDE (degrees)
40N
20
EQ
20
40S
160W
120
80
40
GM
40
80
120
160E
LONGITUDE (degrees)

Figure 14(a

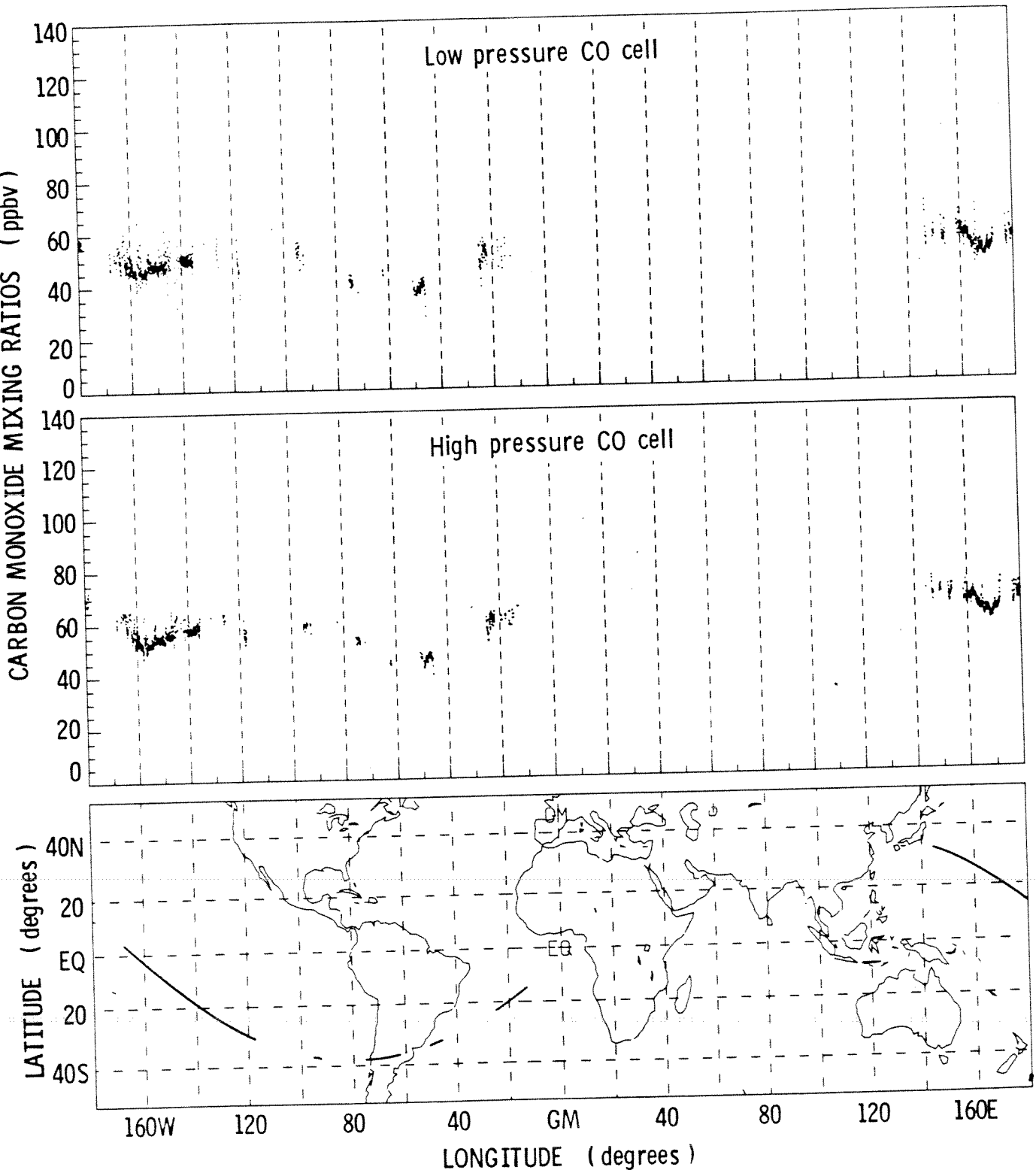
Low pressure CO cell
High pressure CO cell
CARBON MONOXIDE MIXING RATIOS (ppbv)
140
120
100
80
60
40
20
0
LATITUDE (degrees)
40N
20
EQ
20
40S
160W
120
80
40
GM
40
80
120
160E
LONGITUDE (degrees)

Figure 14(b)

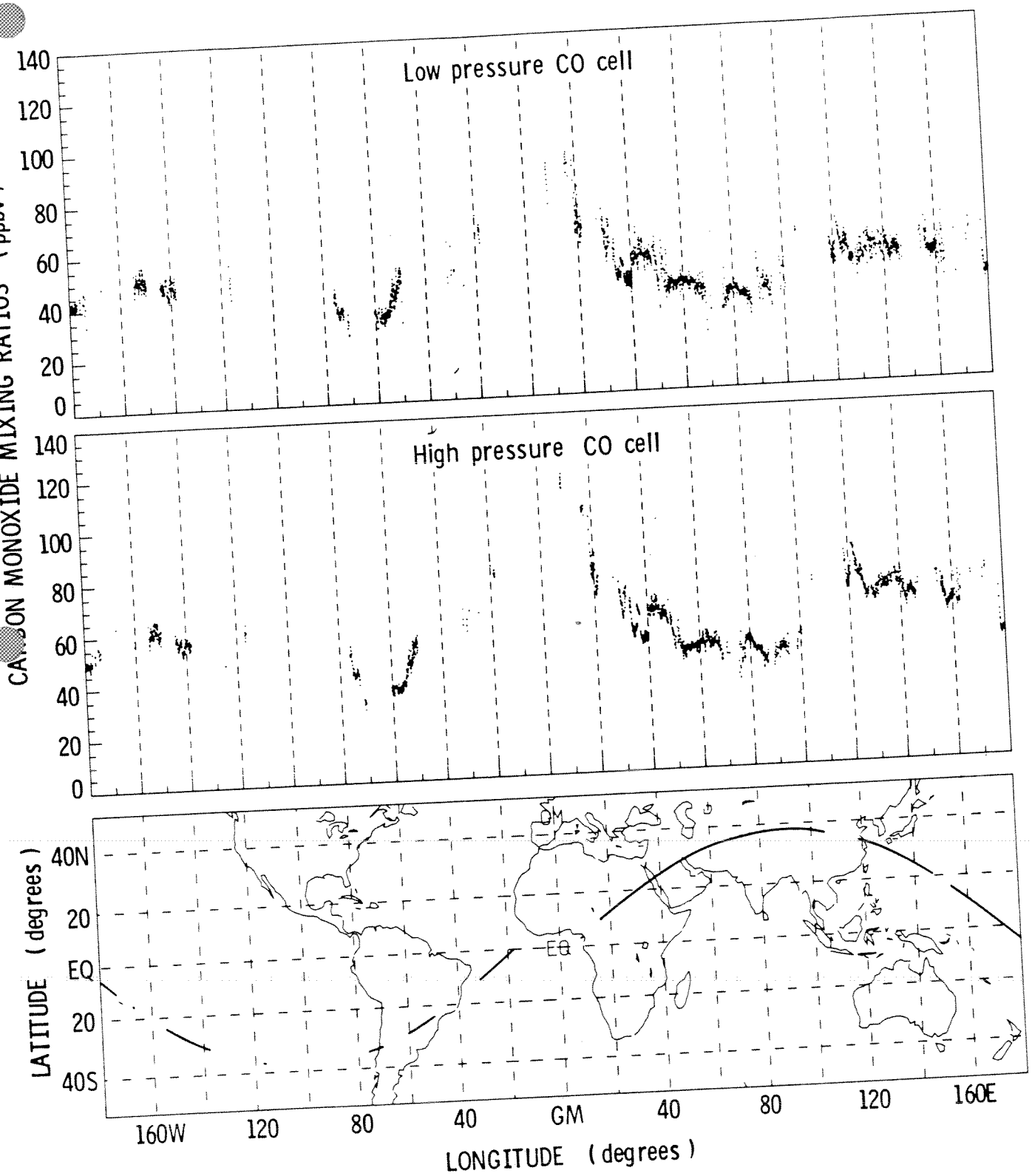
Low pressure CO cell
High pressure CO cell
CARBON MONOXIDE MIXING RATIOS (ppbv)
0
20
40
60
80
100
120
140
LATITUDE (degrees)
40N
20
EQ
20
40S
160W
120
80
40
GM
40
80
120
160E
LONGITUDE (degrees)

Figure 14(c)

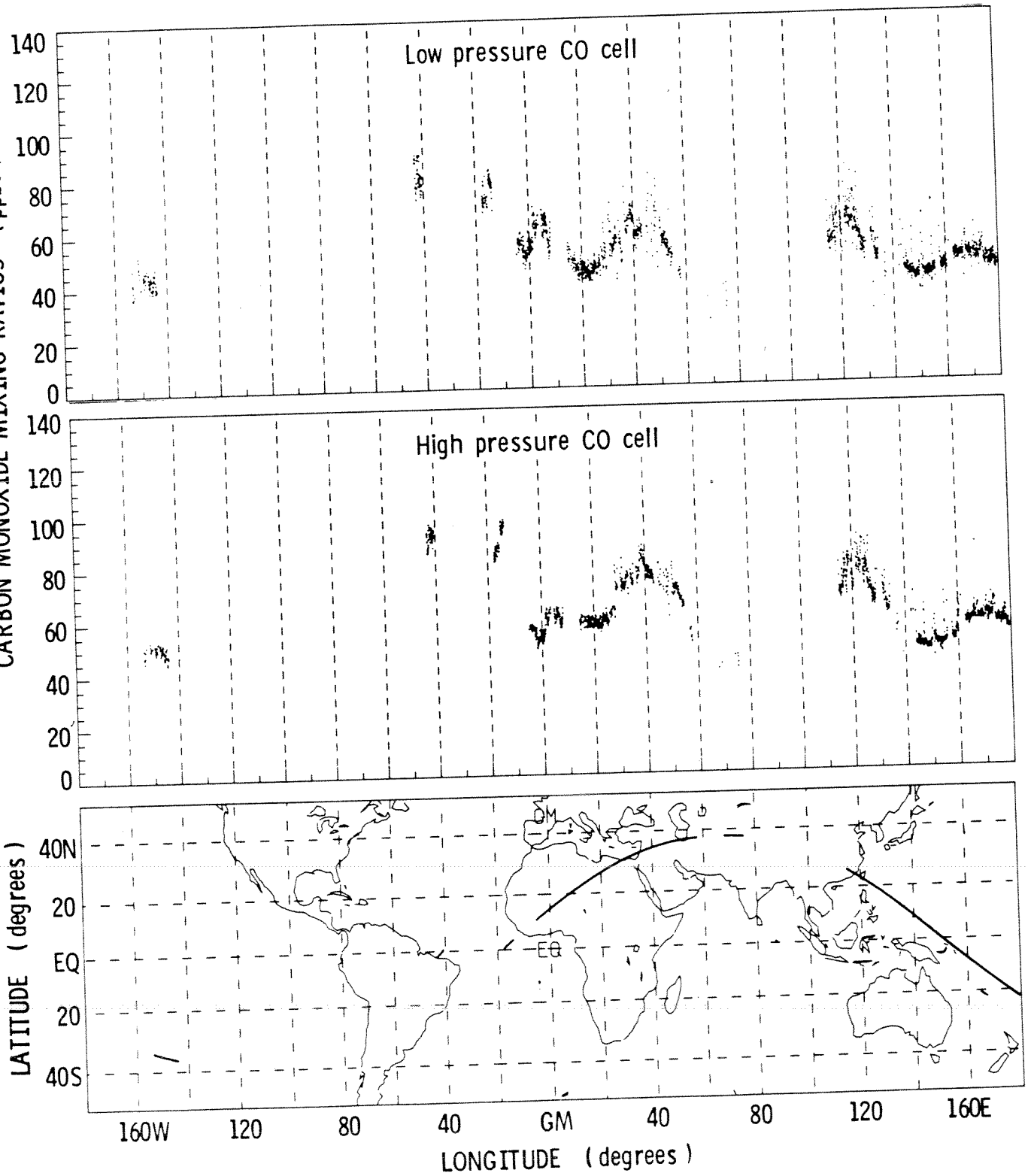
Low pressure CO cell
High pressure CO cell
CARBON MONOXIDE MIXING RATIOS (ppbv)
140
120
100
80
60
40
20
0
LATITUDE (degrees)
40N
20
EQ
20
40S
160W
120
80
40
GM
40
80
120
160E
LONGITUDE (degrees)

Figure 14(d)

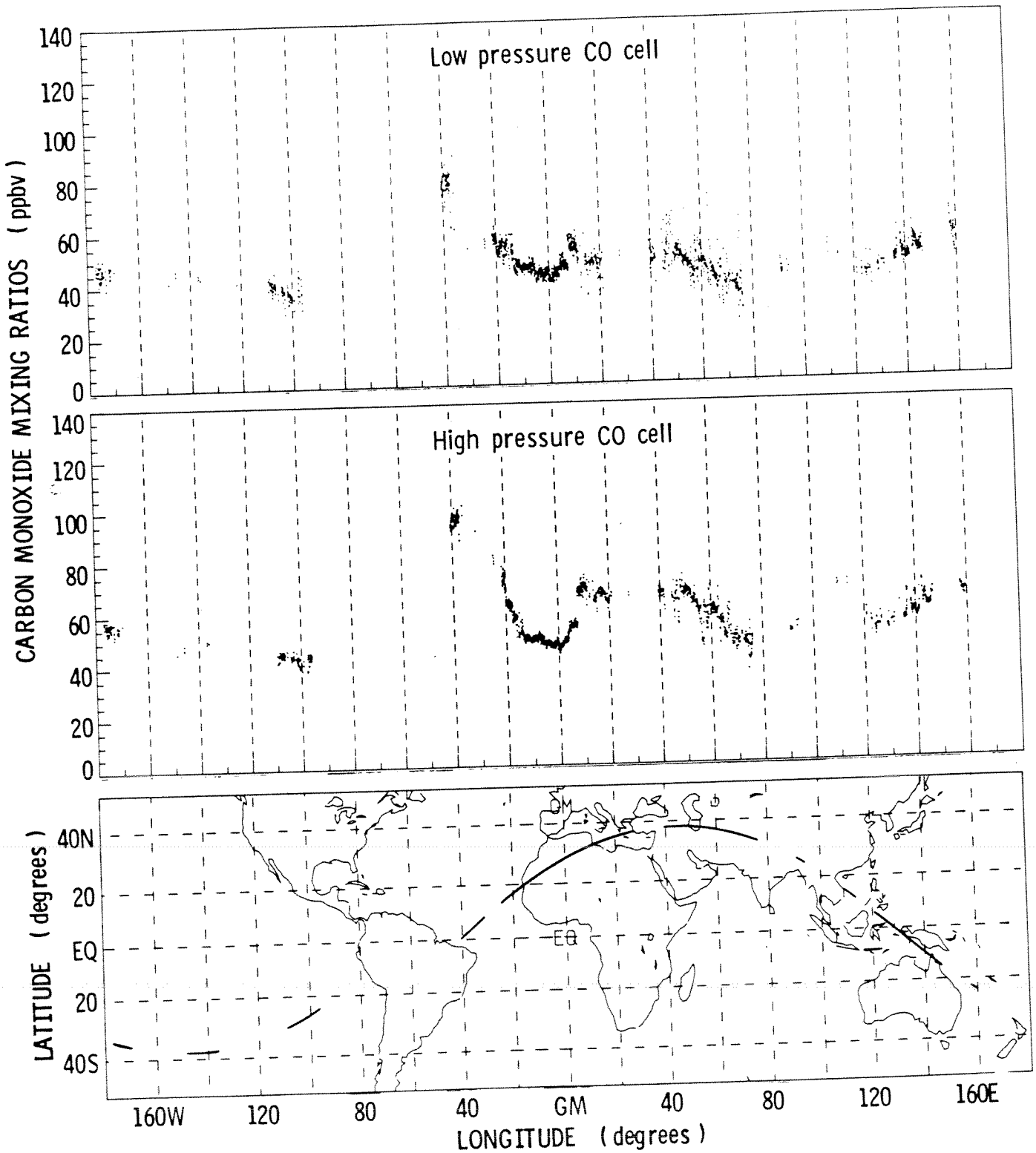
Low pressure CO cell
High pressure CO cell
CARBON MONOXIDE MIXING RATIOS (ppbv)
140
120
100
80
60
40
20
0
LATITUDE (degrees)
40N
20
EQ
20
40S
160W
120
80
40
GM
40
80
120
160E
LONGITUDE (degrees)

Figure 14(e)

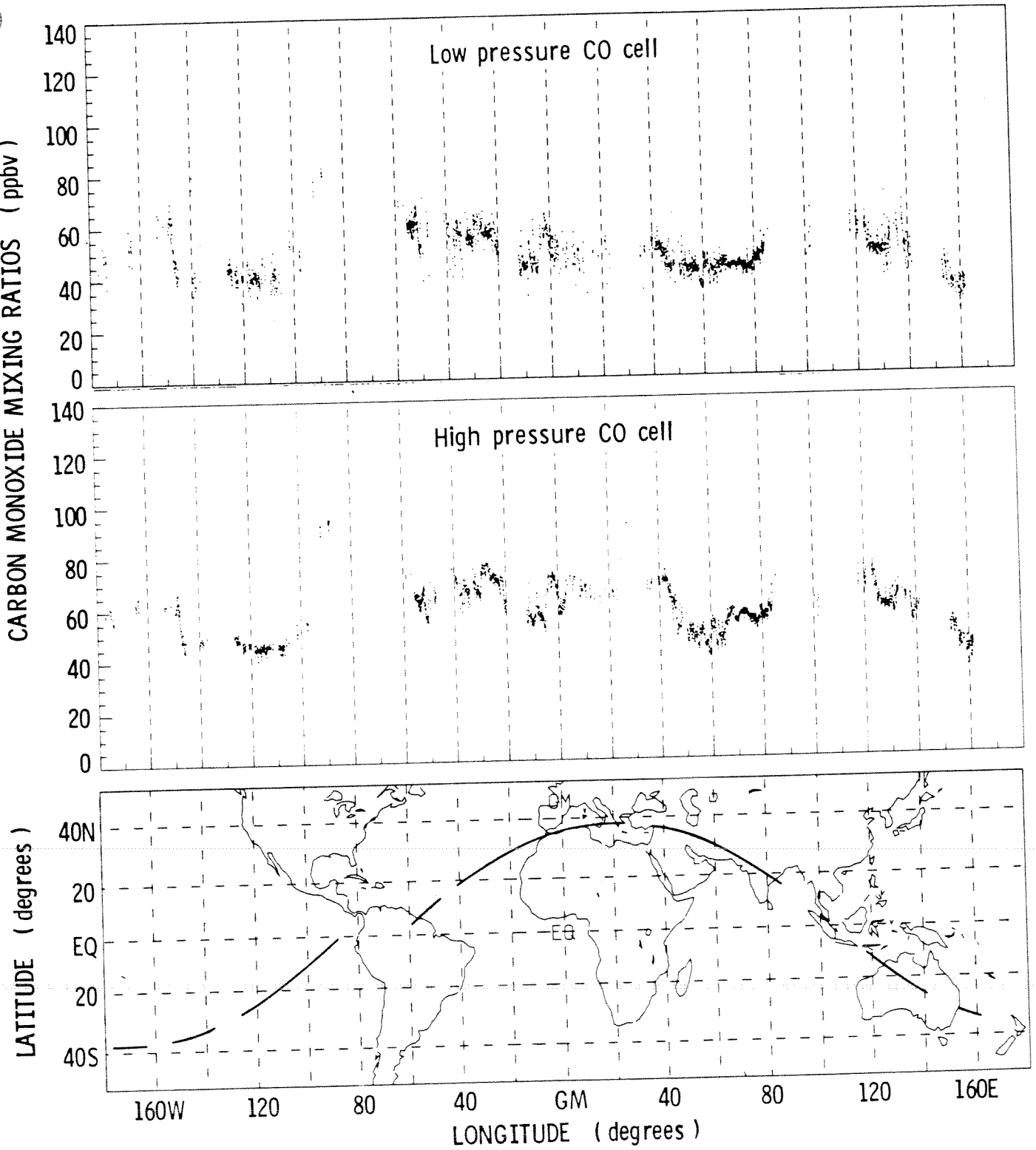
Low pressure CO cell
High pressure CO cell
CARBON MONOXIDE MIXING RATIOS (ppbv)
140
120
100
80
60
40
20
0
LATITUDE (degrees)
40N
20
EQ
20
40S
GM
EQ
160W
120
80
40
GM
40
80
120
160E
LONGITUDE (degrees)

Figure 14(f)

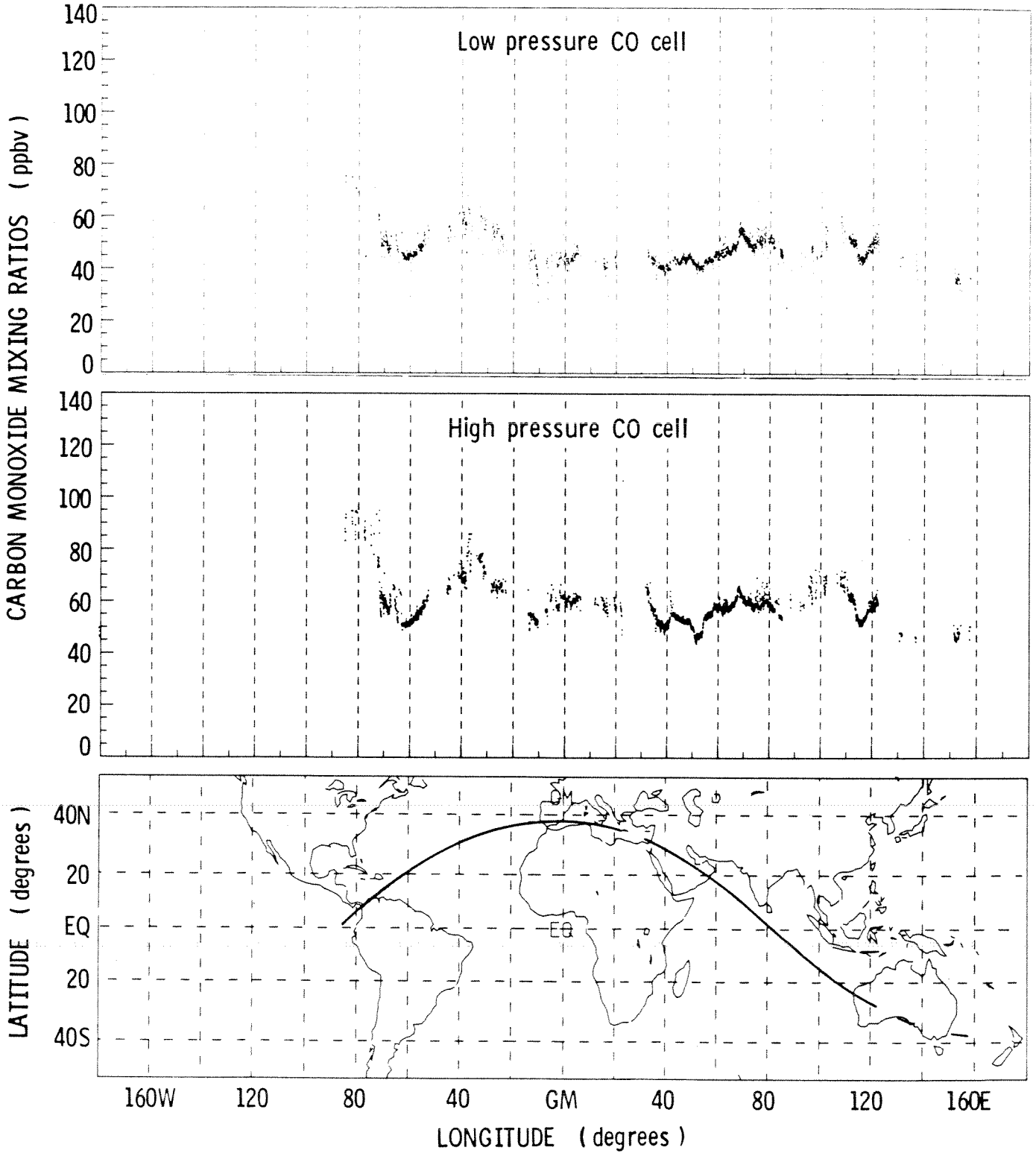
Low pressure CO cell
High pressure CO cell
CARBON MONOXIDE MIXING RATIOS (ppbv)
140
120
100
80
60
40
20
0
LATITUDE (degrees)
40N
20
EQ
20
40S
GM
EQ
160W
120
80
40
GM
40
80
120
160E
LONGITUDE (degrees)

Figure 14(c

Appendix 1

For the V channel, the equation to convert voltage to radiance is

$$L^{\circ} = \frac{[V - (\beta_1 + \beta_2 T)]}{R^V}$$

where V is the V channel voltage, T is the mainframe temperature (TBB2), $R^V = \alpha_1 + \alpha_2 T$, and

$\beta_1 = -1.9602$

$\beta_2 = 5.6953E - 3$

$\alpha_1 = 4.5092E + 5$

$\alpha_2 = -1.1965E + 3$

For the ΔV or $\Delta V'$ channels, the equation to convert voltage to radiance is

$$\Delta L = \frac{[\Delta V - \Delta V_{ref}]}{R^{\Delta V}}$$

where ΔV is the ΔV or $\Delta V'$ channel voltage, T is the mainframe temperature (TBB2), V is the V channel voltage, $R^{\Delta V} = R_1 + R_2 T$, $\Delta V_{ref} = [A_1 + A_2 T + V*(B_1 + B_2 T + B_3 T^2)]$, and

	ΔV	$\Delta V'$
A_1	3.62721	0.1479
A_2	-.011571	0
B_1	-84.98629459	-55.08037
B_2	0.59887702	0.3827556
B_3	-1.05422E - 3	-6.6488E - 4
R_1	1.0832E + 7	1.0392E + 7
R_2	-2.8409E + 4	-2.7466E + 4

DESCRIPTION OF MAGNETIC TAPES

1. Physical record size: 200 characters per record
2. Logical record size: 200 characters per record
3. 9-TRACK tape
4. DENSITY: 1600 bpi
5. UNBLOCKED
6. ODD PARITY
7. UNLABELED
8. ASC II
9. Phase encoding modulation
10. ONE FILE PER TAPE
11. ONE END-OF-FILE PER TAPE

TAPE 1: START TIME: 318:00:58:56 (27478736. seconds)
STOP TIME: 318:06:40:00 (27499200. seconds)

TAPE 2: START TIME: 318:06:40:01 (27499201. seconds)
STOP TIME: 318:13:30:00 (27523800. seconds)

NUMBER OF RECORDS: TAPE 1 - 20252
TAPE 2 - 24347

The data are written with 200 characters per record. The format for reading the records is as follows:

```
      READ (X,N) TIME, TER, LAT, LONG,
     *           V, DV, DVP,
     *           TBB1, TBB2, TBB4,
     *           TBB5, TBB6, TREF,
     *           SZN, DNSFT, DNPSFT,
     *           N, DN, DNP, CO1, CO2,
     *           LW, STWD, CDST

      N FORMAT (F10.0, F8.0, 2(F9.2), 3(F8.4), 6(F8.2),
     *          3(F7.1), 5(E12.4), I5, 2(I3))
```

NOTE: INTEGER NUMBERS: LW, STWD, CDST

REAL NUMBERS: ALL OTHER VARIABLES

VARIABLE DESCRIPTION:

TIME (F10.0) Time of day in seconds
TIME = DAY * 86400 + HOUR * 3600
+ MINUTES * 60 + SECONDS

TER (F8.0) Mean topographic elevation or bathymetric depths in meters
POSITIVE For Land
NEGATIVE For Water

LAT (F9.2) Degrees

LONG (F9.2) Degrees

V (F8.4)	Measured signal output for the V channel in volts
DV (F8.4)	Measured signal output for the ΔV channel in volts
DVP (F8.4)	Measured signal output for $\Delta V'$ channel in volts
TBB1 (F8.2)	Temperature of controlled internal reference blackbody in degrees Kelvin
TBB2 (F8.2)	Temperature of internal balance blackbody in degrees Kelvin
TBB4 (F8.2)	Temperature of the external calibration blackbody in degrees Kelvin
TBB5 (F8.2)	Temperature of the external balance cold blackbody in degrees Kelvin
TBB6 (F8.2)	Temperature of the external balance hot blackbody in degrees Kelvin
TREF (F8.2)	Temperature of the reference cal cell in degrees Kelvin
SZN (F7.1)	Solar zenith angle in degrees
DNSFT (F7.1)	The signal function weighted atmospheric temperature for the ΔV channel in degrees Kelvin
DNPSFT (F7.1)	The signal function weighted atmospheric temperature for the $\Delta V'$ channel in degrees Kelvin
N (E12.4)	Calculated radiance value for the V channel in watts cm^{-2} SR^{-1}

DN (E12.4) Calculated radiance value for the ΔV channel in watts cm^{-2} sr^{-1}.

DNP (E12.4) Calculated radiance value for the ΔV' channel in watts cm^{-2} sr^{-1}.

CO1 (E12.4) Inferred CO mixing ratio for the ΔV channel in parts per billion by volume.

CO2 (E12.4) Inferred CO mixing ratio for the ΔV' channel in parts per billion by volume.

LW (I5) Code for terrain type

0 - All positive land

2 - Significant lake included

3 - Contains ice - (no process)

4 - Contains ice (no process)

5 - Contains land and ocean

8 - Contains some land below sea level

9 - All ocean

STWD (I3) Instrument and mirror status word

STWD = 25 Calibrate/cool balance
= 26 Calibrate/warm balance
= 27 Calibrate/calibrate
= 58 Operate/scene (DATA MODE)
All else mirror moving.

CDST (I3) Inferred CO status word

CDST = 0 Cloud free
= 1 Cloud contaminated
= 2 V channel saturation
= 3 NO TSF data (ZLV off)
= 4 N threshold

CDST (13) Inferred CO status word (Concluded)

CDST = 5 TSF out range

= 6 Terrain type 3 or 4

= 7 CO threshold CO < 0 or CO $\geq$ 240

= 8 Fallout reason

= 9 Calibrate cycle

```
$NOP
$NOP
$NOP ********* SIN-3 **************
$EXE TPLIST BS

INPUT PARAMETERS ARE:  AS FL=5=5 1 1

 TAPE NO.    1              FILE NO.    1
 RECORD    1                LENGTH    2 3
 27478736.  -5200.    -37.46      1.84 -4.5600    .6000    .5800  318.33  283.57  310.49  280.05  320.3
2  290.84  110.4  245.9  240.0    .9346E-05    .1989E-06    .1543E-06    .7905E-07    .8324E-07     9 58
 1

 TAPE NO.    1              FILE NO.    1
 RECORD    2                LENGTH    2 3
 27478737.  -5200.    -37.45      1.92 -4.6100    .5900    .5700  318.37  283.57  310.49  280.05  320.3
2  290.84  110.4  245.9  240.0    .8956E-05    .1964E-06    .1503E-06   -.9990E+03   -.9990E+03     9 58
 4

 TAPE NO.    1              FILE NO.    1
 RECORD    3                LENGTH    2 3
 27478738.  -5200.    -37.44      1.99 -4.6700    .5600    .5400  318.41  283.57  310.49  280.05  320.3
2  290.84  110.4  245.9  240.0    .8476E-05    .1870E-06    .1386E-06   -.9990E+03   -.9990E+03     9 58
 4

 TAPE NO.    1              FILE NO.    1
 RECORD    4                LENGTH    2 0
 27478739.  -5100.    -37.43      2.07 -4.7300    .5100    .5100  318.44  283.57  310.49  280.05  320.3
2  290.84  110.4  245.9  240.1    .7994E-05    .1704E-06    .1270E-06   -.9990E+03   -.9990E+03     9 58
 4

 TAPE NO.    1              FILE NO.    1
 RECORD    5                LENGTH    2 0
 27478740.  -5100.    -37.42      2.15 -4.7800    .4500    .5000  318.48  283.57  310.49  280.05  320.3
2  290.84  110.6  245.9  240.1    .7596E-05    .1500E-06    .1230E-06   -.9990E+03   -.9990E+03     9 58
 4

 TAPE NO.    1              FILE NO.    1
 RECORD  20248              LENGTH    2 0
 27499195.  -5200.    -18.54  -163.17 -5.1100    .1300    .2900  318.37  282.64  310.61  280.05  320.3
6  290.56  117.1  253.0  245.2    .4948E-05    .3492E-07    .2968E-07   -.9990E+03   -.9990E+03     9 58
 2

 TAPE NO.    1              FILE NO.    1
 RECORD  20249              LENGTH    2 0
 27499196.  -5200.    -18.57  -163.11 -5.1100    .1200    .2900  318.35  282.64  310.61  280.05  320.3
6  290.56  117.1  253.0  245.2    .4924E-05    .3135E-07    .2968E-07   -.9990E+03   -.9990E+03     9 58
 2

 TAPE NO.    1              FILE NO.    1
 RECORD  20250              LENGTH    2 0
 27499197.  -5200.    -18.61  -163.06 -5.1100    .1000    .2800  318.33  282.64  310.61  280.05  320.3
6  290.56  117.1  253.0  245.2    .4900E-05    .2422E-07    .2588E-07   -.9990E+03   -.9990E+03     9 58
 2

 TAPE NO.    1              FILE NO.    1
 RECORD  20251              LENGTH    2 0
 27499198.  -4800.    -18.65  -163.00 -5.1100    .1200    .2900  318.32  282.64  310.61  280.05  320.3
6  290.56  117.1  253.0  245.2    .4877E-05    .3135E-07    .2968E-07   -.9990E+03   -.9990E+03     9 58
 2

 TAPE NO.    1              FILE NO.    1
 RECORD  20252              LENGTH    2 0
 27499199.  -4800.    -18.69  -162.95 -5.1100    .1100    .2900  318.30  282.64  310.61  280.05  320.3
```

5TB-2/OSTA-1
81-111A-04A
D-72286
C-25945